AEROSOL SCIENCE AND TECHNOLOGY
2025, VOL. 59, NO. 5, 544–566
https://doi.org/10.1080/02786826.2024.2412652

Influence of relative humidity and aging on the optical properties of organic aerosols from burning African biomass fuels

Megan M. McRee[a†], Vaios Moschos[b,c], Marc N. Fiddler[d], Dario Massabò[e,f], Jason D. Surratt[b,g], and Solomon Bililign[a,c]

[a]Department of Applied Sciences and Technology, College of Science and Technology, North Carolina A&T State University, Greensboro, North Carolina, USA; [b]Department of Environmental Sciences and Engineering, Gillings School of Global Public Health, The University of North Carolina at Chapel Hill, Chapel Hill, North Carolina, USA; [c]Department of Physics, College of Science and Technology, North Carolina A&T State University, Greensboro, North Carolina, USA; [d]Department of Chemistry, College of Science and Technology, North Carolina A&T State University, Greensboro, North Carolina, USA; [e]Department of Physics, University of Genoa, Genoa, Italy; [f]National Institute for Nuclear Physics (INFN), University of Genoa, Genoa, Italy; [g]Department of Chemistry, College of Arts and Sciences, The University of North Carolina at Chapel Hill, Chapel Hill, North Carolina, USA

ABSTRACT

Biomass burning (BB) is a major source of atmospheric fine carbonaceous aerosols, which play a significant, yet uncertain, role in modulating the Earth's radiation balance. However, accurately representing their optical properties in climate models remains challenging due to factors such as particle size, mixing state, combustion type, chemical composition, aging processes, and relative humidity (RH). In our study, we investigated BB organic-rich aerosols generated from smoldering sub-Saharan African biomass fuels. Fuel samples were collected in Africa and aerosols generated in the laboratory. We quantified key optical parameters, including mass cross-sections for extinction (2.04 ± 0.32 – 15.5 ± 2.48 m^2/g), absorption (0.04 ± 0.01–0.3 ± 0.1 m^2/g), and scattering (1.9 ± 0.68–15.3 ± 5.5 m^2/g). Wavelength-dependent properties were used to determine absorption and scattering Ångström exponents. The single scattering albedo of these aerosols ranged from 0.8 ± 0.03 to 1.0 ± 0.04 and we observed a wavelength-dependent behavior. Extinction emission factors were determined at a wavelength of 550 nm, with values ranging from 42 ± 5 to 293 ± 32 m^2/kg. Notably, optical properties exhibited fuel-type dependence, with differences observed between hardwood samples and other fuels, such as grass and animal dung. Aging increased mass extinction and scattering cross-sections at 550 nm, while humidity had the opposite effect across all fuels. Nitrate radical oxidation, both in photo and dark aging conditions, also influenced these properties. The findings are expected to close the gap in our understanding of optical properties of BB aerosol emissions in one of the least studied regions of the world – Africa – providing information to climate and air quality models for the region.

GRAPHICAL ABSTRACT

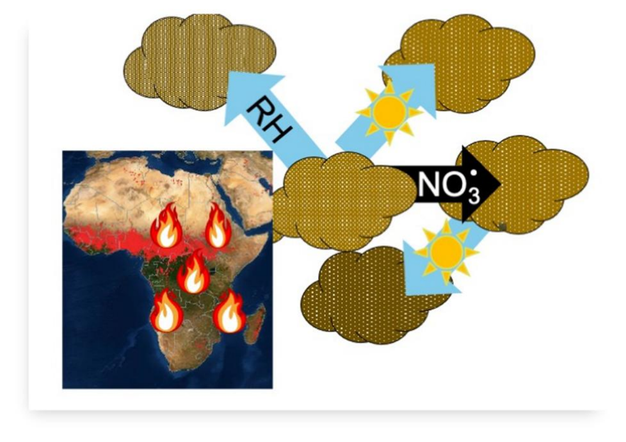

ARTICLE HISTORY
Received 30 June 2024
Accepted 25 September 2024

EDITOR
Hans Moosmüller

CONTACT Solomon Bililign bililignsol@gmail.com; bililign@ncat.edu North Carolina A&T State University, 1601 E. Market St. Greensboro, NC 27411, USA.

Supplemental data for this article can be accessed online at https://doi.org/10.1080/02786826.2024.2412652.

[†]Formerly Megan Mouton.

1. Introduction

Biomass burning (BB) aerosols with aerodynamic diameters $<2.5\,\mu$m, which we refer to as "fine" aerosol in this article are airborne particles with aerodynamic diameters $<2.5\,\mu$m that are emitted during domestic use of biomass fuels, clearing of forests for agriculture, prescribed fires, and wildfires (Andreae 2019; Bond et al. 2013). Fine BB aerosols impact air quality and potentially human health upon inhalation (Andreae 2019). Fine aerosols directly absorb or scatter solar radiation, reducing visibility and altering global and regional radiative forcing (Hamilton et al. 2018; Thornhill et al. 2018). In addition, they can indirectly affect the climate system by acting as cloud condensation nuclei (CCN) as well as altering cloud properties and lifetimes, and thus, changing precipitation patterns (Cecchini et al. 2017).

Africa accounts for approximately 72% of the burned area worldwide as well as approximately 52% of the carbon emissions, including 44% of carbon monoxide (CO), 36% of methane (CH_4), and 60% of total black carbon (BC) emissions (Ichoku 2020; Ichoku et al. 2016; van der Werf et al. 2010). Recent estimates show that Africa's fire emissions are 31–101% higher than previously estimated (Ramo et al. 2021). Africa may significantly contribute to future carbon emissions that affect the global atmospheric composition as they will occur in the tropics, where they will have more influence on atmospheric oxidation and radiative forcing (Crutzen and Andreae 1990, 2016; Santos et al. 2018). It is shown that long-range transport of BB smoke plumes significantly alters their chemical composition and optical characteristics due to aging (Konovalov et al. 2021). Therefore, there is a need to understand these emissions not just for their effect on the population of Africa, but for global climate and air quality. However, only a few studies have investigated the impact of aerosols from African BB on the global radiative budget, (Andreae 2019; Bond et al. 2013; Brown et al. 2021). The influence of African biomass fuel type on optical properties has not been investigated in controlled laboratory studies (Laris et al. 2021).

Recently, there has been a growing interest in understanding the impact of organic aerosol (OA), especially brown carbon (BrC) aerosol components known to absorb more at shorter wavelengths (Akagi et al. 2011; Chen and Bond 2010; Kirchstetter, Novakov, and Hobbs 2004; McMeeking et al. 2009). Studies have shown that the contribution of BrC to total absorption is comparable to or higher than that of other known atmospheric absorbers like BC and mineral dust (Bluvshtein et al. 2017; Flores et al. 2012; Jacobson 2014; Lavi et al. 2017; C. Li et al. 2015, 2016; Moschos 2021; Moschos et al. 2018; Saleh, Cheng, and Atwi 2018; Z. Wang et al. 2017) and contributes significantly to positive radiative forcing, with up to 20% of total aerosol absorption (Feng, Ramanathan, and Kotamarthi 2013; Hems et al. 2021; A. Zhang, Wang, et al. 2020). Despite vigorous efforts, our understanding of the optical properties of BrC-containing OAs remains incomplete. Due to a broad variability in the chemical composition, mixing state, and transformations of OA during atmospheric aging, aerosol optical properties span a wide range of values (Moschos et al. 2018). Given that aerosol particles from smoldering combustion contribute to around 75% of the total global carbonaceous aerosol mass, accurate integration of the optical characteristics of OA into models is crucial for the Earth's radiation budget (Chakrabarty et al. 2010). Furthermore, BC and OA are often emitted into the atmosphere together, making it difficult to isolate OA to characterize its optical properties (Kondo et al. 2011; Moschos et al. 2021). The source of OA also has an impact on aerosol optical properties (X. Wang et al. 2014). West et al. (2020) showed OA from car emissions has a much lower mass absorption cross-section (MAC) than OA emitted from BB. The distinction between primary and secondary OA is often blurred by atmospheric aging of aerosol particles through multi-phase chemical reactions and aerosol microphysical processes (Kroll et al. 2015; Moschos et al. 2018).

A high variability in atmospherically relevant burning conditions has also resulted in a high variability in the reported OA optical properties. This poses a challenge for accurately representing the OA impact on climate. This uncertainty has led climate models to assume that a single constant imaginary part of the refractive index (k) value for OA, specifically for BrC, applies globally (Feng, Ramanathan, and Kotamarthi 2013; Lin et al. 2014; X. Wang et al. 2014). Lee et al. (2018) reported in a remote sensing study that optical properties of wildfire-induced fine aerosols were affected by regional ecosystem types and terrestrial environments. During airborne measurements in the Fire Influence on Regional to Global Environments and Air Quality (FIREX-AQ) field campaign in the western United States (Zeng et al. 2022), significant variability was observed for BrC particles from wildfires in the initial hours of smoke evolution, followed by a decrease in BrC content in plumes 15–30 h old.

To determine the optical properties of BB-derived aerosols, one needs to consider the factors that affect these properties, such as fuel type, burning conditions, morphology, aging, mixing state, chemical composition, size distribution, and meteorological conditions such as relative humidity (RH).

Burning conditions directly affect the aerosol optical properties due to differences in morphology and chemical composition of the emitted aerosols (Hamilton et al. 2018; X. Liu et al. 2008; Pokhrel et al. 2020). For example, flaming-dominated burns produce fractal-like BC (Evangeliou et al. 2019), whereas smoldering-dominated burns mainly produce spherical-like particles that largely consist of organic compounds (Kirchstetter, Novakov, and Hobbs 2004). These burning conditions are also influenced by fuel moisture, which prolongs burns and causes less efficient combustion (Chen and Bond 2010).

RH is another critical parameter that influences aerosol optical properties by causing changes on the morphology of particles (Brock et al. 2016; Cheng et al. 2008; Hand and Malm 2007; Mouton et al. 2023). This is of particular significance for African-derived BB aerosols in (sub-)tropical regions with elevated RH.

Atmospheric aging of OA influences its light-absorbing properties. Aqueous-phase chemical studies on secondary OA constituents reported rapid photobleaching within minutes to hours, suggesting that secondary-OA absorption could have short atmospheric lifetimes (Hems and Abbatt 2018; Lee et al. 2014; Wong, Nenes, and Weber 2017; Wong et al. 2019; Zhao et al. 2015). However, aqueous-phase chemical studies of primary BB-derived OA (BBOA) (Wong, Nenes, and Weber 2017; Wong et al. 2019) suggest that these aerosols have longer lifetimes, and in some cases are even resistant to photoaging. Sumlin et al. (2017) and Browne et al. (2019) reported that BBOA experiences a period of photo enhancement before photobleaching (Wong, Nenes, and Weber 2017; Wong et al. 2019; Zhong and Jang 2014). Under high-nitrogen oxide ($NO_x = NO + NO_2$) conditions, photobleaching of OA has been reported to slow down or cease altogether (C. Li et al. 2019; Zhong and Jang 2014). High-NO_x conditions can occur in polluted urban air environments adversely affected by BB emissions, resulting in the significant production of nitrate (NO_3) radicals during the night that can oxidize OA, and thus, enhance the absorbing properties of BBOA. For example, C. Li et al. (2019) reported that the absorption of BBOA from wood tar more than doubled after 13.3-h of nighttime NO_3 radical aging in laboratory studies. Tandem flow reactor experiments by C. Li et al. (2020) found that NO_3 radical reactions increased the light absorption of wood tar aerosols; however, under daytime conditions their absorption decreased. More studies are needed so that optical properties of nighttime BBOA aging can be better characterized. The number of atmospheric studies of the nighttime aging of BBOA are limited, leading to uncertainties in models (X. Wang et al. 2018).

Our laboratory study presented herein is focused on OA generated from smoldering burning of African biomass fuels. We report laboratory measured values of several aerosol optical parameters, including the mass extinction cross-section (MEC), measured mass scattering cross-section (MSC_{Meas}), mass absorption cross-section (MAC), mass scattering cross-section calculated as a difference between MEC and MAC (MSC_{Calc}), absorption Ångström exponent (AAE), scattering Ångström exponent (SAE), and single scattering albedo (SSA). We also systematically investigated the dependence of these optical parameters on fuel type, aging conditions, RH, and on oxidation conditions in the laboratory. In addition, we report extinction emission factors (EEFs) as it aids in evaluating the emission intensities of pollutants (Tian et al. 2019). Results are compared with measurements from smoldering combustion of biomass fuels from other continents.

2. Experimental details

The experimental setup for this work is shown in Figure 1, with a slight deviation from the setup used by Mouton et al. (2023). Fuels were burned in a tube furnace and the smoke was introduced into a 9-m^3 Teflon environmental chamber in the lab at North Carolina Agricultural and Technical State University (NC A&T University) in Greensboro, NC. This experimental setup was previously used to measure the emission factors (EFs) as well as the optical properties of aerosols generated from burning African biomass fuels (Moschos et al. 2024; Mouton et al. 2023; Pokhrel et al. 2020, 2021; Smith et al. 2019). Filter samples were also collected for chemical analysis of BrC aerosol constituents at University of North Carolina at Chapel Hill (UNC-Chapel Hill), with details published elsewhere (Moschos et al. 2024; Smith et al. 2020). Subsequent sections below provide a brief description of determination of fuel moisture

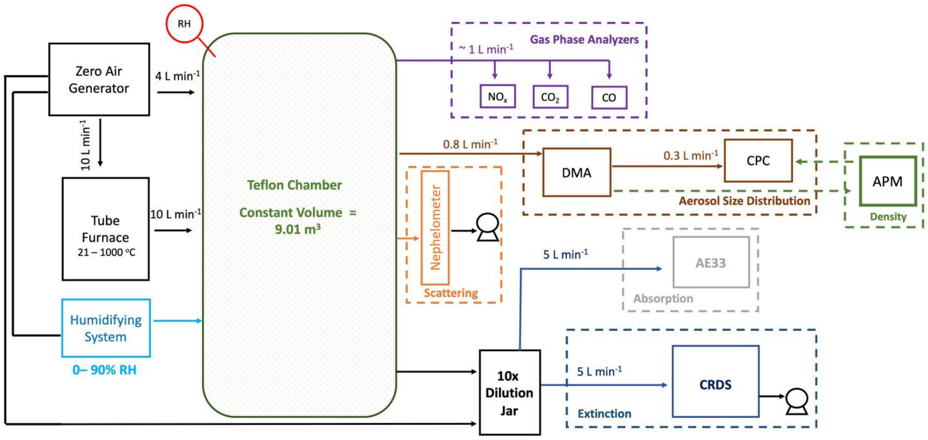

Figure 1. Schematics of the experimental setup for OA optical property measurements.

Table 1. Fuels and their moisture contents used for experiments.

Common name	Scientific name	Origin	Moisture (%)
Bahir Zaf/Eucalyptus	*Eucalyptus camaldulensis*	Botswana	$<10\%$
Acacia	*Acacia Abyssinica*	Botswana	3.4 ± 0.7
Wanza	*Cordia Africana*	Ethiopia	$<10\%$
Mukusi/African teak	*Baikiaea plurijuga*	Botswana	3.4 ± 0.6
Mopane/balsam tree	*Colophospermum mopane*	Botswana	$<10\%$
Ethiopian cow dung	*n/a*	Ethiopia	$<10\%$
Mosetlha	*Peltophorum africanum*	Ethiopia	4.5 ± 1.4
African fountain grass/Savannah grass	*unknown*	Botswana	$<10\%$
Mokala	*Acacia erioloba*	Ethiopia	4.0 ± 1.2
Wild olive	*Olea europaea*	Botswana	2.8 ± 1.0
Mopane leaves	*Colophospermum mopane leaves*	Botswana	7.8 ± 1.3

content, fuel burning condition, operating conditions of the chamber, chamber humidification, oxidation conditions, optical extinction, scattering and absorption measurements, and statistical analysis.

2.1. Sub-Saharan African fuels, fuel moisture and burning conditions

African biomass fuels obtained directly from Ethiopia, Kenya and Botswana were burned under a variety of burning conditions, as quantified by the modified combustion efficiency (MCE). The fuels selected are representative of those burned for domestic use in Africa (Beyene and Koch 2013). Fuel samples were stored in a fume hood to dry. Fuel moisture content was measured at New Mexico Tech employing a moisture analyzer (PCE-MA 50x). The analyzer first measured the initial sample weight and dried the fuel, providing the moisture content, temperature, and time profile for each sample. Finally, it calculated the mean, standard deviation, and coefficient of variation for each sample. The measured moisture content is shown in Table 1 along with the fuel names and their geographical location. The moisture content of the other fuels in the list was estimated to be less than 10% (Pokhrel et al. 2020). Based on the measured moisture content fuels were sufficiently dry.

To produce BB aerosols, ~0.5 g of fuels was burned in a tube furnace (Carbolite Gero, HST120300-120SN) for each experiment. Fuels were placed in a quartz boat (AdValue Technology, FQ-BT-03) at the center of the preheated tube furnace after it was preheated to the desired temperature of 450 °C. Particle-free filtered air (Aadco Instruments, 747-30) was introduced into the furnace at 10 L min^{-1} using a calibrated mass flow controller (MFC, Sierra Instruments). All aerosols and gases produced from combustion passed through a cyclone (URG, URG-2000-30ENS-1) to select fine particles smaller than 2.5 μm before they were introduced to the Teflon chamber.

CO (Thermo Scientific 48iQ Carbon Monoxide Analyzer) and CO$_2$ (Thermo Scientific410iQ Carbon Dioxide Gas Analyzer) were measured for all burns and were used to determine the MCE, (Yokelson, Griffith, and Ward 1996) defined as:

$$MCE = \frac{\Delta CO_2}{\Delta CO + \Delta CO_2} \tag{1}$$

All MCE values measured from our experiments fall within ranges indicative of smoldering dominated conditions (MCE < 0.9), and they were achieved by setting the tube furnace to a lower temperature of 450 °C. We have previously demonstrated that by using a tube furnace we can dial in to a specific burning condition and MCE (Pokhrel et al. 2020) in order to measure optical properties as a function of burning condition and determine if the aerosol composition is mostly OA or BC (Smith et al. 2019).

2.2. Operating conditions of the chamber

The indoor environmental fixed-volume (i.e., 9.01 m^3) chamber was operated in batch mode and thus, was maintained under positive constant pressure to minimize the inflow of contaminated room air. The chamber was initially filled with particle-free filtered air from our zero-air generator (Aadco Instruments, 747-30). A mixing fan was activated before combustion and remained on for the entire experiment. Once the aerosol number or volume distribution was stabilized. (as measured by the scanning mobility particle sizer (SMPS); Sect. 2.6), which typically occurred within ~30 min from the time of combustion, the chamber was considered well mixed. The chamber maintained a constant flow of zero air to counterbalance the continuous sample flow rates by the instruments. Details of the characterization and construction of the indoor chamber are reported elsewhere (Smith et al. 2019). Smith et al. (2019) also reported particle wall losses at a rate of $9.46 \times 10^{-3}\,\mathrm{min}^{-1}$ for aerosol mass concentration, and we measured a wall loss rate of $2.5 \times 10^{-3}\,\mathrm{min}^{-1}$ in our experiments, which is the same order of magnitude to the earlier results.

2.3. Chamber humidification

The humidification process of the chamber was described in Mouton et al. (2023). Briefly, particle-free air flowed through a customized bubbler (Quark Glass) containing approximately 400 mL of deionized water (i.e., American Society for Testing and Materials (ASTM) Type II water with less than 50 ppb of total organic carbon). The heated bubbler was attached periodically when changes in RH were desired, resulting in approximately 2% RH change when vapor was introduced for 2–3 min. RH and temperature were monitored with a Hygrometer/Thermometer (VWR). We conducted experiments under two different conditions: dry conditions with an RH of 0–10% and humid conditions with a RH value of 60–75%.

2.4. Aging conditions

Three types of aging experiments were conducted in this study. Dark aging representing nighttime emissions under dry conditions, where fresh emissions were kept for three hours in the chamber. Photoaged samples are exposed to UV light for 1–1.5 h. Details of the UV lights are described in our previous work (Smith et al. 2019), specifically the light source used were 30- Watt UVA, 356 nm centered spectrum, 36 in (length), F30T8/350BL/ECO, Sylvania. The same procedure is repeated under humidified conditions (~70% relative humidity). Oxidation experiments are conducted in a humidified chamber (~70% RH), where NO_2 and O_3 were introduced to form NO_3 radicals before combustion. Aging conditions and sampling stages are similar as before. This is described in greater detailed in Section 3.1.

2.5. Ozone and NO_x injection

Throughout the initial phase of the experiments, the slow reaction between ozone (O_3) and nitrogen dioxide (NO_2) generated nitrate (NO_3) radicals as both gases were introduced into the chamber (Fry et al. 2011; Rollins et al. 2009). This setup was designed to investigate the nighttime chemistry involving NO_3 radicals. The experiments were initially conducted in the dark to simulate nocturnal conditions, followed by photo-aging measurements (see Figure 2b).

To conduct dark aging experiments with NO_3 radicals, NO_2 was first introduced into the chamber until it reached approximately 500 ppbv. Subsequently, O_3 was introduced using an ozone generator (Model L21, Pacific Ozone). This generator was fed with 5 SCFH of 95% pure O_2 and set to produce 10% O_3. The generator operated for about 30 s until the O_3 concentration reached 200 ppbv. Once O_3 and NO_2 levels stabilized after 1 h, we began measurements due to the expectation of NO_3 radical production.

Based on the concentrations of NO_2 and O_3 used, we estimated that ~ 250 pptv of NO_3 radicals were initially present. The applicable rate constants, according to the IUPAC value of $1.4 \times 10^{-13} e^{-\frac{2470}{T}}$ where T is the temperature in Kelvin, indicated that NO_3 primarily dominates the initial oxidation (Hamilton et al. 2021; Surratt et al. 2008). Considering that average ambient NO_3 levels are around 10–60 pptv (Hamilton et al. 2021), our initial experimental conditions are higher. Similarly, our aerosol concentrations reached approximately 1000 $\mu g\ m^{-3}$, whereas normal ambient aerosol measurements range from 20 to 80 $\mu g\ m^{-3}$ (Health Effects Institute 2020). This elevated

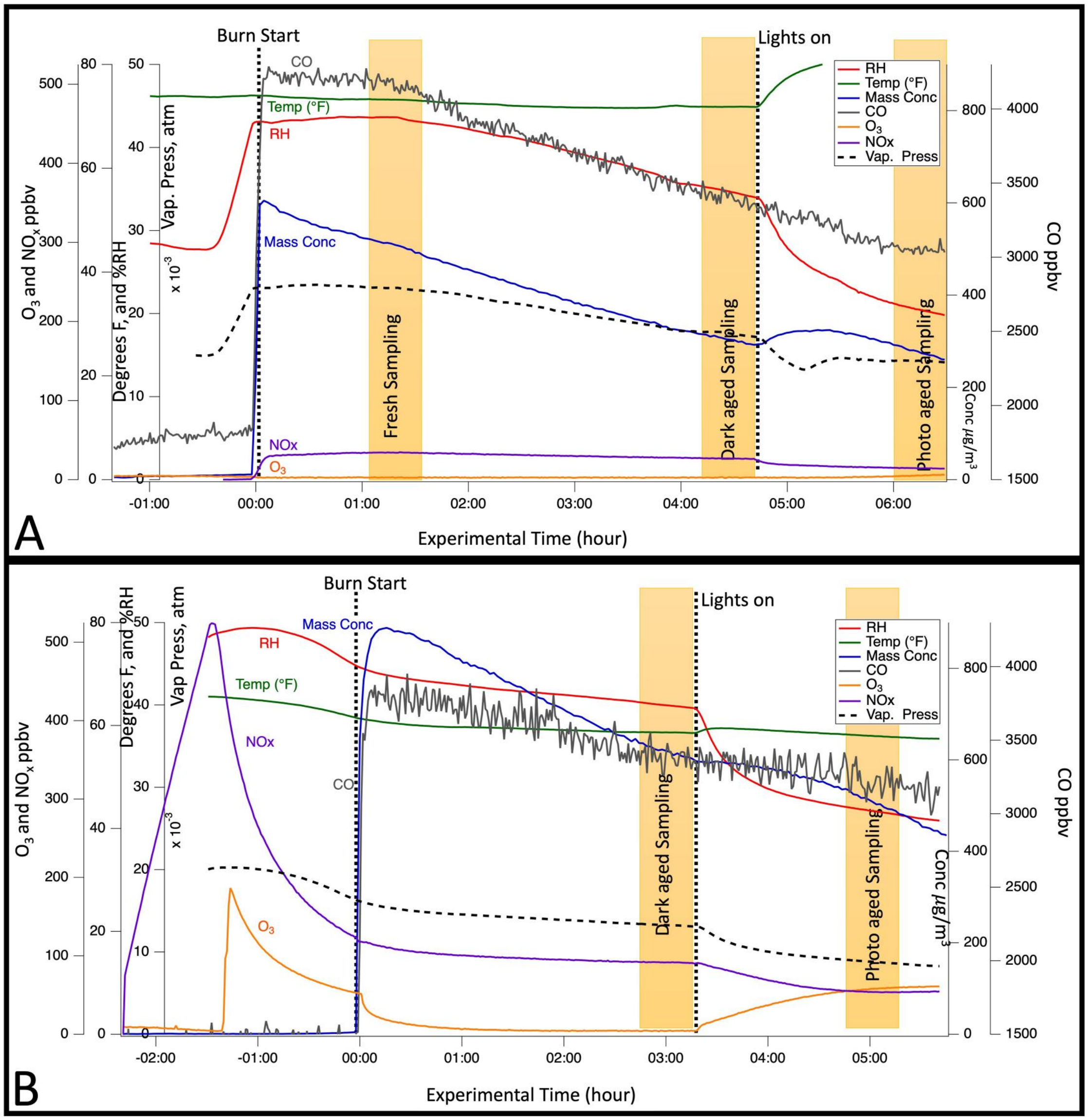

Figure 2. Typical experimental time series. The example shown is from the burning of Ethiopian cow dung, which examined the effects of RH, aging, and oxidation conditions. Humidified control experiments (a) and those undergoing NO_3 radical oxidation (b) are shown in terms of NO_x, O_3, CO, RH, temperature, and particle mass concentration. The dotted black line is the calculated partial pressure of water. Burn and light start times are distinguished by dashed black lines, and sampling times are indicated with yellow rectangles in both figures.

concentration helps ensure that the gas and heterogeneous oxidation reactions with NO_3 radicals occurs on the timescale of our experiments.

2.6. Gas phase, aerosol size, aerosol mass, and optical property measurements

From the chamber, gas species, including O_3 (2B Technologies, Model 211 Scrubber less Ozone Monitor) and NO_x (Thermo Scientific 42iQ NO-NO_2-NO_x Analyzer), and aerosols were sampled. The aerosol size distributions were measured using SMPS. Specifically, aerosol particles passed through an impactor inlet with a cut point of 3.8 μm (particle diameter) before entering a long differential mobility analyzer (DMA, TSI model 3080). Aerosols sized by the DMA were counted by a water-based condensation particle counter (WCPC, TSI model 3788) in order to measure the aerosol number concentrations. The mass concentration M represents the total mass of particles per unit volume of air sampled in µg m^{-3}. The calculation assumes that particles are perfect spheres, which is a practical approximation for smoldering-dominated burns in this work (Kirchstetter, Novakov, and Hobbs 2004; Pokhrel et al. 2020). The mass is related to particle diameter as:

$$M = \rho \sum \left(N \frac{\pi}{6} D_p^3 \right) \tag{2}$$

Where N represents the aerosol number concentration (particles m^{-3}) at a specific diameter, D_p is the geometric diameter at a specific particle size, and ρ is the effective particle density (g cm^{-3}). Particle size distributions were corrected for multiple charging using in-software calculations. Density measurements were conducted using a tandem configuration consisting of an aerosol particle mass analyzer (APM, Kanomax model 3602) in conjunction with our DMA. For all the experiments and experimental conditions (fuel type, aging condition and RH levels) the measured density ρ remained constant at 1.2 ± 0.1 g cm^{-3}.

Mie's theory describes the scattering of electromagnetic radiation by spherical particles and applying it to smoke particles requires consideration of deviations from spherical shape, since a minor deviation from perfect sphericity can impact calculations (Koop et al. 2011; D. Liu et al. 2014). However, under smoldering conditions as in our experiments, smoke particles tend to exhibit a near-spherical shape, that justifies the use of Mie theory (Pokhrel et al. 2020) for comparing with values in literature.

A cavity ringdown spectrometer (CRDS) was used to measure extinction of light by particles at a wavelength of 550 nm (Equation (S2)). Aerosol sampled from the chamber entered a ring-down cavity (170 cm long, stainless steel, ½" OD), for measuring light extinction. The laser system consists of a Continuum Surelite I-20 Nd: YAG laser operating at 20 Hz. The 355-nm beam pumps an optical parametric oscillator (OPO). Details of the CRDS and setup can be found in previous work (Singh, Fiddler, and Bililign 2016; Singh et al. 2014; Smith et al. 2019). We provide the equation for extinction coefficient using CRDS in Equation (S1) (Moosmüller, Varma, and Arnott 2005; Smith et al. 2019; Strawa et al. 2006; Thompson, Smith, and Winefordner 2002; Thompson et al. 2008). During our experiments, sampling from the chamber was conducted with a dilution jar to decrease the aerosol concentrations to prevent saturating the CRDS. The flow rate for the cavity was 5 L min^{-1}, the dilution flow from the chamber to the CRDS was 4.5 L min^{-1} producing a dilution rate of 90%, and the purge flow on the cavity was about 50 mL min^{-1}.

Using the calculated extinction coefficient from the CRDS and the scattering coefficient measured at wavelength of 453,554 and 698 nm obtained from the Nephelometer (TSI Model 3563), MEC and MSC_{Meas} values were calculated respectively using Equation (3) in (m^2 g^{-1});

$$MEC = \frac{\alpha_{ext}}{M_{pm,\,crds}} \tag{3}$$

Where α_{ext} (m^{-1}) is the extinction coefficient, and $M_{pm,\ crds}$ is the mass concentration of aerosol in the CRDS. For calculating MSC values, Equation (3) was used with α_{scat} (m^{-1}) which is the scattering coefficient and the mass concentration of aerosol in the chamber $M_{pm,\ cham}$, instead of $M_{pm,\ crds}$. MSC is also calculated as the difference between MEC and MAC, and the calculated values are designated as MSC_{calc} (m^2 g^{-1}).

The calibration of the nephelometer followed the procedure outlined in a previous study (Singh et al. 2014), but with a slight modification. Both the nephelometer and the CRDS were calibrated with polydisperse ammonium sulfate aerosol particles achieving a size distribution comparable to that in our BB experiments. Since ammonium sulfate aerosol particles are completely scattering, the nephelometer readings had to match the value of extinction (scattering + absorption) measured using CRDS. As such, the truncation angle correction of Anderson and Ogren (1998) and a wavelength-independent correlation factor was applied to nephelometer α_{scat}.

The light absorption properties of aerosols were determined using a dual spot aethalometer (AE33, Magee Scientific). The AE33 assesses the passage of light through segments of the filter tape containing the sample (I) and compares it to the light transmission through an empty spot acting as a reference (I_O), to estimate the optical attenuation at seven wavelengths (λ), ranging from 950 to 370 nm. The attenuation coefficient, $a_{attn.}$, was estimated as the light attenuation rate of change passing through a particle-laden filter (Magee Scientific 2016). A multi-wavelength absorbance analyzer (MWAA) (Massabò et al. 2013, 2015) was utilized to obtain wavelength-specific calibration coefficients for the AE33 attenuation coefficients and approximate the aerosol absorption coefficients, following the approach originally described in Moschos et al. (2021). The determination of AE33 calibration coefficients for AE33 wavelengths was based on adjacent-wavelength absorption Ångström exponents, which assumed a power-law relationship. Dimensionless calibration coefficients were applied to correct absorption coefficients for apparent absorption caused by scattering artifacts, including multiple scattering effects. In this process, we estimate the approximate absorption coefficient for all samples and assume that MWAA measurements are closer to the true absorption value The MWAA measures the transmission and backward scattering at two fixed angles, which considers the scattering contributions to attenuation. The details of the calculation and calibration for these specific chamber aerosol samples are provided in Moschos et al. (2024).

We calculated the extinction emission factor (EEF, $m^2\ kg^{-1}$) in this work. EEF is defined as:

$$\begin{aligned} &EEF = EF*\ MEC \\ &Where\ \ EF = \frac{M_{peak}\left(g\ \ m^{-3}\right)volume_{chamber}\left(m^3\right)}{mass_{burned}(kg)} \end{aligned} \tag{4}$$

EEF is a key factor in determining the environmental impact of BB emissions, which quantifies the extinction burden resulting from different fuels. M_{peak} represents the peak mass concentration of particles within the chamber minus the small mass present before the burn.

SSA is the ratio of mass scattering coefficient to total mass extinction coefficient. SSA is an essential parameter used to determine direct radiative forcing (DRF) of aerosols. Errors in MEC and MSC_{Meas} measurements could yield nonphysical SSA values exceeding 1 when scattering and extinction measurements are close. However, this is specific to mostly organic and highly scattering aerosols at 550 nm wavelength. The extinction minus scattering technique based on CRDS and nephelometer applied to flaming conditions were consistent with values in the literature (Pokhrel et al. 2016; Smith et al. 2020). This suggests that the validity of the SSA measurement using extinction minus scattering is dependent on the burning condition. We used two equations to determine SSA. Equation (5) that used extinction (CRDS) and absorption (AE33) measurements,

$$SSA = \frac{MEC - MAC}{MEC} \tag{5}$$

or using the scattering (nephelometer) and the absorption (AE33) measurements for determining SSA_{alt}, using Equation (6)

$$SSA_{alt} = \frac{MSC}{MSC + MAC} \tag{6}$$

Absorption and scattering Ångström exponents were calculated using Equations (S2) and (S3).

2.7. Statistical analysis

A two-sample mean, one-tailed t-test was used for statistical analysis to demonstrate if the results were statistically significant. This method determines whether the observed differences between the means of two groups or results are likely due to a real effect or merely by chance. By using this test, the presence of statistical significance of the measured values in this work, was determined. The error bars in all the results represent one standard deviation between mean values from repeated experiments (i.e., the run-to-run variability). There were two repeated experiments for all fuels, except Mosethla and Savanna grass which had three experiments.

3. Results and discussion

The results of MEC and MSC_{Calc} measurements for all 11 fuels in all experiments are provided in Table S1. The EEFs and changes in optical properties due to changes in humidity, aging conditions (photoaging, dark aging with and without NO_3 radical oxidation), burning condition (MCE), and wavelength are examined and discussed following the details of the experimental time series for the measurements conducted.

3.1. Experimental time series

Three aging experiments were conducted; (1) to represent nighttime emissions (both fresh and then dark aged without NO_3 radicals intentionally added) followed by photoaging (using UV lights in the chamber as described in Smith et al. (2019)) under dry conditions, (2) the same as in (1) under humidified conditions, and (3) to represent dark aging/oxidation by NO_3 radicals in the humid chamber, followed by photoaging. During most experiments (Figure 2), it took approximately 10 min for the fuel to fully burn and the smoke (gases and particles) was introduced into the chamber and left to mix for an additional 50 min. One hour after injecting the fresh BB emissions, initial aerosol sampling took ~30 min. The fresh aerosol particles were then left to age in the dark for ~3 h, followed by another 30-min aerosol sampling period. Lastly, chamber lights were switched on that allowed the BB emissions to photochemically age for ~1–1.5 h, followed by another 30-min aerosol sampling period.

In the humidified control (i.e., no oxidation by NO_3 radicals) experiment (Figure 2a), the chamber was humidified to approximately 70% RH before initiating the burn. Burn and mixing time were the same as above. Sampling times for the fresh, dark aged, and photochemically aged samples were like the dry conditions.

During the oxidation experiments (Figure 2b), the chamber was humidified to ~70% RH. Burn and mixing times and sampling stages were the same as above. In both cases, the indoor chamber temperature monitored was room temperature, which showed a slight seasonal and daily variation between winter and summer when most of the experiments were done.

In Figure 2a, we observe a rapid decrease in RH during dark aging sampling, followed by a swift return to a stable level. Conversely, in Figure 2b, toward the end of the experiments when the lights were switched on, the RH diminishes to half of its initial level. Additionally, there is a decline in RH at the start of burning, which is expected due to the introduction of new particles, and again when the lights were turned off. The drop observed in Figure 2b was notably more pronounced compared to Figure 2a. Figure S1 represents the particle number distribution across the three aging periods corresponding to the experiments depicted in Figure 2.

At the start of the experiments, the RH was generally 70 and 75% in Figures 2a and b, respectively, while the temperature ranged from 18 to 26 °C. After the smoke was injected into the chamber, both type of experiments showed an increase in NO_x levels, which then quickly stabilized. Subsequently, there was a general decline in NO_x, especially once the lights were turned on. Upon switching on the chamber lights, significant changes were observed in both experiments. There was a rapid decrease in RH, with the increase in temperature, and an elevation of aerosol mass concentration that was indicative of secondary organic aerosol (SOA) formation. In Figure 2a, there was a slight decrease in NO_x levels, while O_3 levels remained constant throughout the experiment. CO showed a slight decrease. In Figure 2b, there were steady NO_x levels, especially after the initial period of $NO_2 + O_3$ reactions, followed by an increase in O_3 due to NO_2 photolysis upon turning on the lights. CO slightly decreased throughout both experiments likely due to chamber dilution. Experimental time series were similar for other fuels, and an additional time series are shown in Figure S2 for Mopane.

3.2. Impact of RH on aerosol optical properties of fresh (primary) BBOA

RH affects the aerosol optical properties of BBOA generated from the smoldering combustion of these African biomass fuels. This study explored the influence of humidity on MEC, MSC_{Calc}, and MAC of these BB aerosols, as summarized in Figure 3. Magi and Hobbs (2003) measured the total light scattering coefficient as a function of RH across several locations in southern Africa downwind from wildfires. This prior study utilized a humidified nephelometer system and found that for aged smoke from tropical Africa there was a decrease in MSC_{Calc} with an increase in RH. The MSC_{Calc} determined from this prior study showed a similar trend with our measurements, where both MEC and MSC_{Calc} decreased with increasing RH.

Specifically, MEC ranged from 4.0 ± 0.64 to $15.5 \pm 2.48\,m^2\ g^{-1}$ under dry conditions (0–10% RH) and ranged between 2.0 ± 0.32 and $7.9 \pm 1.3\,m^2\ g^{-1}$ under RH conditions (60–75% RH). Using a paired two-sample t-Test, we calculated a one-tailed p-value of 6.7×10^{-3}, indicating a probability of 0.67% that the observed impacts of RH on MEC was a coincidence. The MSC_{Calc} ranged from 4.0 ± 0.64 to $15.3 \pm 5.50\,m^2\ g^{-1}$ under dry (0–10% RH) conditions and ranged between 1.9 ± 0.68 and $7.6 \pm 2.73\ m^2\ g^{-1}$ under elevated RH. By using a paired two-sample t-Test, we calculated a one-tailed p-value of 0.0068, indicating a probability of 0.68% that the observed impacts of photochemical aging on MSC_{Calc} was a coincidence. Finally, for MAC under dry conditions (0–10% RH) values ranged from 0.03 ± 0.01 to $0.3 \pm 0.1\ m^2\ g^{-1}$, and 0.04 ± 0.014 to $0.2 \pm 0.07\,m^2\ g^{-1}$ under RH conditions (60–75% RH). The average decrease from dry to high RH measurements was $2.3\,m^2\ g^{-1}$ for MEC and $2.2\,m^2\ g^{-1}$ for MSC_{Calc}, nearly the same decrease. The largest difference was found for Mosetlha where the dry and humid MEC was $16 \pm 3\,m^2\ g^{-1}$ and $7 \pm 1\ m^2\ g^{-1}$, respectively.

In the African tropics, where RH can range from as low as 39% to as high as 98% (Akinbode, Eludoyin, and Fashae 2008), the influence of moisture on the optical properties of BBOA is significant (Yoon and Kim 2006). Our laboratory studies indicated a decrease in BBOA particle extinction in the presence of humidity, a trend supported by field studies (Magi and Hobbs 2003). Similarly, Marsavin et al. (2023) investigated BBOA aerosols during the 2021 Oregon fire season, comparing wildfires and prescribed fires. They observed that prescribed fires, occurring under RH conditions due to land preparation and moistening, yielded aerosols with a MSC_{Calc} only 1.05 times higher than that of aerosols from wildfires. This finding is not aligned with our observations of impact of RH on MSC_{Calc}. Furthermore, studies have shown that the hygroscopicity of aerosols is correlated with their optical properties (Xia et al. 2023). For example, OAs can undergo hygroscopic growth when

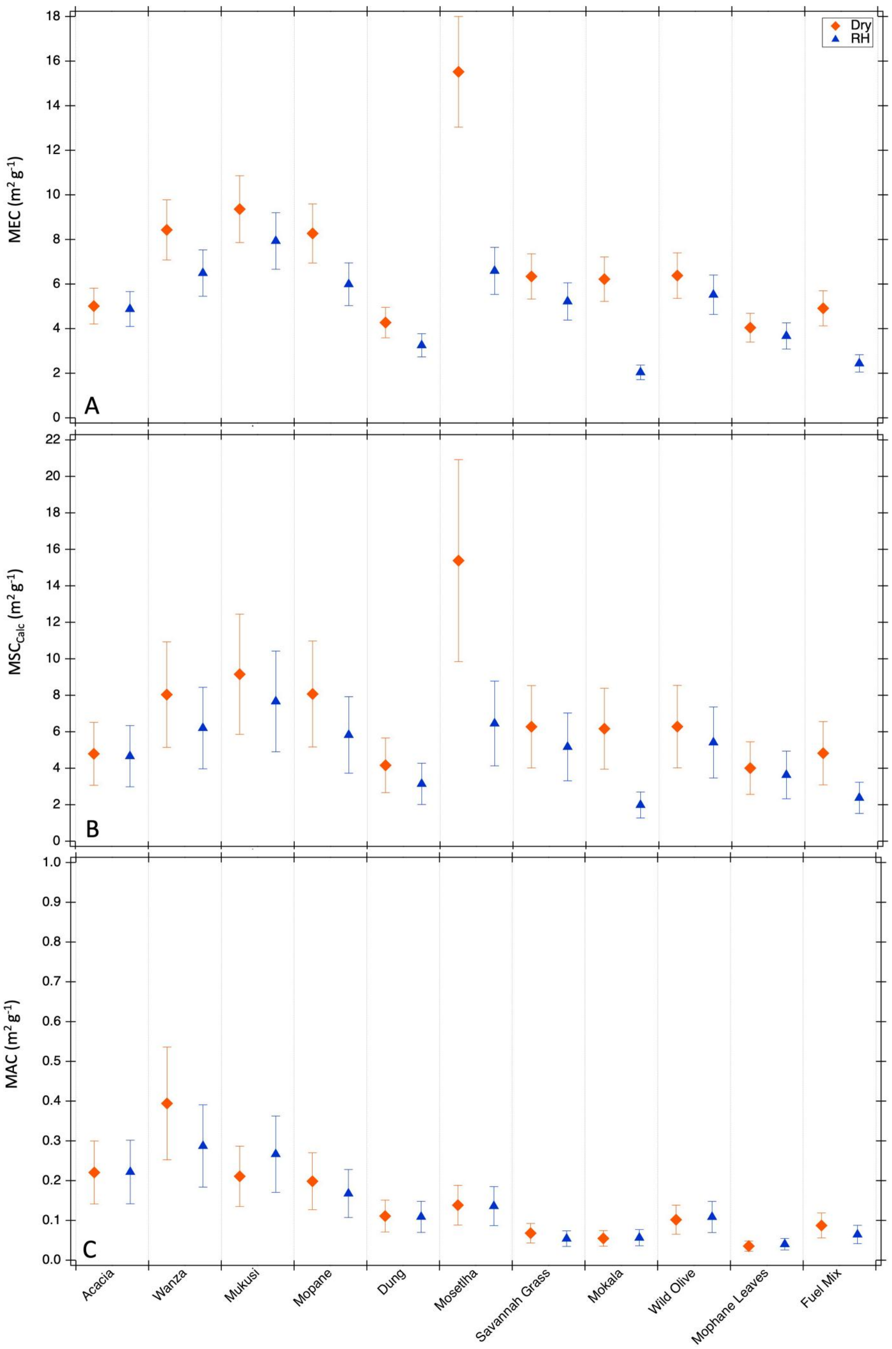

Figure 3. Effect of RH on MEC (a), MSC_{Calc} (b), and MAC (c). Orange diamonds represent dry measurements (0–10% RH) and blue triangles represent humid measurements (60–75% RH) of primary BBOA particles. The fuel types are listed along the x-axis. The error bars depicted on the figures represent one standard deviation between repeat measurements.

interacting with atmospheric water vapor, leading to size increases and alterations in optical properties (Jianhua et al. 2023; Jin et al. 2022; Q. Liu et al. 2020; Mouton et al. 2023). This growth hardly changes the optical absorption efficiency due to dilution effects from water uptake, as demonstrated by Lack and Langridge (2013) in their investigation of BB aerosols. Thus, these findings underscore the intricate relationship between aerosol composition, humidity, and optical properties.

3.3. Impacts of photochemical aging on aerosol optical properties of African (primary) BBOA

Figure 4 illustrates the impact of photochemical aging on MEC and MSC_{Calc} values. The MEC and MSC_{Calc} values of aerosols resulting from smoldering-dominated combustion of African fuels exhibit an increase due to photochemical aging, except for Mosetlha. The experiment was intended to represent aerosol from fires that occur at night, age physically through the

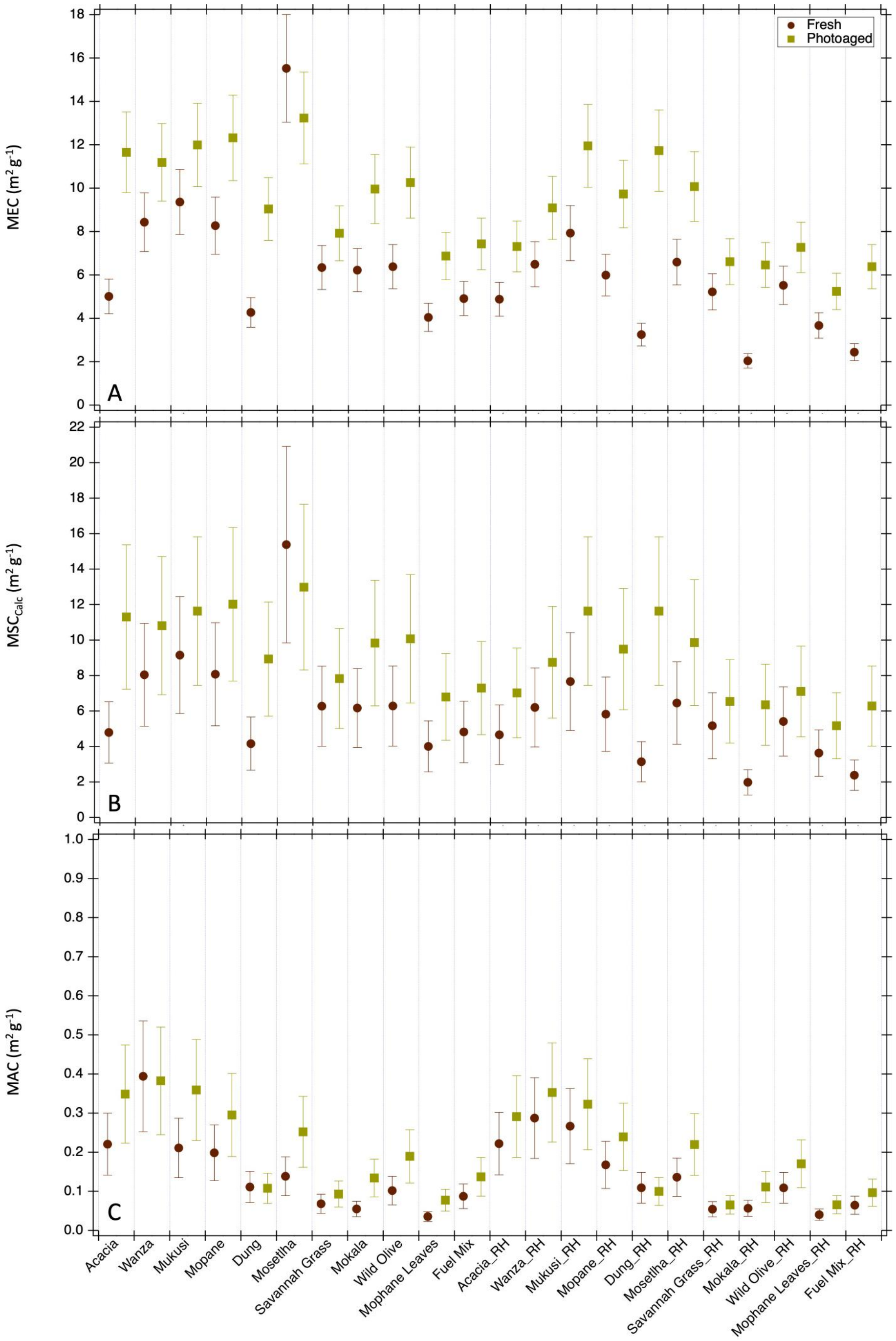

Figure 4. Photochemical aging of most African BBOA types increases MEC (a), MSC$_{Calc}$ (b), and MAC (c) values. Brown circles indicate average fresh measurements and green squares indicate average photochemically aged measurements. The fuel types are listed along the x-axis. The error bars depicted in the figures represent one standard deviation between multiple measurements. The maximum relative standard deviation was 16%, 36%, 36% for MEC, MSC$_{Calc}$, and MAC respectively.

night, and are then exposed to daylight (with no additional NO_3 radical). This aging leads to increased aerosol extinction and scattering. Photochemical aging could also lead to lower volatility organic products condensing onto preexisting BBOA, consequently shifting the aerosol size distribution to larger sizes (Shilling et al. 2019). Additionally, chamber walls can cause smaller and more thermally diffusive particles to be lost, which would make the larger (accumulation mode) particles stand out more (Jain et al. 2021). Lastly, chamber dilution could cause semi-volatile species in smaller particles (with their higher surface-to-volume ratio) to evaporate to smaller sizes that are then lost to the chamber walls (Jain et al. 2021). Typical chamber data shown in Figure 2a show that photochemical aging led to increased aerosol mass concentrations due to the production of SOA from gas-phase organic species that undergo some combination of gas-phase oxidation chemistry, aerosol-phase chemistry, and vapor pressure driven partitioning. This secondary processing can affect extinction by changing the optical properties per unit mass and by changing the aerosol mass.

The fresh MEC values ranged from 2.0 ± 0.32 to 15.5 ± 2.48 $m^2\ g^{-1}$, while the photochemically aged MEC values ranged from 5.2 ± 0.83 to 13.2 ± 2.11 $m^2\ g^{-1}$. Additionally, the fresh MSC_{Calc} values ranged from 1.9 ± 0.68 to 15.3 ± 5.50 $m^2\ g^{-1}$, while the photochemically aged MSC_{Calc} values ranged from 5.1 ± 1.8 to 12.9 ± 4.6 $m^2\ g^{-1}$ (as shown in Table S1). Finally, the fresh MAC values ranged from 0.03 ± 0.01 to 0.3 ± 0.10 $m^2\ g^{-1}$, and the photochemically aged MAC values ranged from 0.06 ± 0.21 to 0.3 ± 0.10 $m^2\ g^{-1}$. In Figure 4a, the most significant impact of photochemical aging was evident in the MEC for Dung, showing an increase from 4.2 ± 0.67 to 8.9 ± 3.2 $m^2\ g^{-1}$. The least pronounced effect of photochemical aging was observed in the MEC for Savannah grass, with a modest total increase of 1.3 $m^2\ g^{-1}$. Using a paired two sample for mean t-Test, we found a one tail p-value of 1.65×10^{-7} suggesting a statistically significant effect of photochemical aging. A consistent outlier in Figure 4 was Mosetlha, where the MEC was 16 ± 2.56 $m^2\ g^{-1}$ for its fresh emission and decreased to 13 ± 2.08 $m^2\ g^{-1}$ when photochemically aged. Mosetlha had a MSC_{Calc} value of 15.3 ± 5.50 $m^2\ g^{-1}$ for fresh aerosol and decreased to 12.9 ± 4.64 $m^2\ g^{-1}$ when photochemically aged. The experiment was repeated to confirm the outlier behavior. The same t-Test found a one-tailed p-value of 4.3×10^{-9} for the observed impacts of photochemical aging on MSC_{Meas}. Photoaging led to an increase in both the MEC and MSC_{Calc} with average difference for MEC is 3.2 and MSC_{cal} is 3.1. The results were reproducible with little variability between experiments, as shown by the size of the error bars in the figures.

The optical properties of BBOA have been the subject of extensive research, with studies examining their light-absorption characteristics and the factors influencing them. Lu et al. (2015) observed periodic variations in the MAC of BrC in BB aerosols, with an increase during the morning hours followed by a decline. These findings were corroborated through laboratory experiments (Wong, Nenes, and Weber 2017; Wong et al. 2019; Zhao et al. 2015), highlighting the impact of UV exposure and OH radical reactions on aerosol light absorption. Their investigations revealed intricate relationships between photochemical processes and the optical properties of BBOA. Specifically, they demonstrated that UV exposure induces chemical transformations within BBOA particles, leading to changes in their absorptive properties over time. Moreover, aging due to the presence of OH radicals in the atmosphere further influenced aerosol light absorption characteristics (Browne et al. 2019; Paulson et al. 2019). Several studies highlight the significance of aging processes in modifying the optical properties of BBOA (Hodshire et al. 2019; Jolleys et al. 2012; Leskinen et al. 2023; J. Liu et al. 2016; Schnitzler et al. 2022; Williams et al. 2018; You et al. 2024). They underscore the crucial role of chemical reactions in altering aerosol absorptivity during aging. By simulating realistic atmospheric aging conditions in controlled laboratory settings, these studies elucidate the dynamic interplay between aging-induced chemical transformations and changes in aerosol optical properties Additionally, Smith et al. (2020) found that photochemical aging of BBOA particles led to an increase in both the extinction and scattering cross sections. This prior study also showed an increase in SSA for fresh Eucalyptus from 0.7 to close to 1 after aging (Smith et al. 2020). Furthermore, Smith et al. (2020) showed that the 300 nm size-selected BB aerosols produced under smoldering-dominated burning conditions became highly scattering after photochemical aging. Using flight data from western US wildfires, Kleinman et al. (2020) showed that average extinction, scattering, and absorption extinction cross-sections increased between fresh and aged measurements. Similarly, our data shows an increase in scattering and extinction with exposure to UV light.

By determining the average particle geometric cross section (Table S2), the effects of a changing particle size distribution can be largely removed. In Figure 5, we show that the extinction efficiencies without the addition of NO_3 radical consistently increase upon dark and then photochemical aging, indicating that these changes are not due to size differences in the particles but with chemical composition changes due to aging. We previously demonstrated compositional differences between the different experiments or aging conditions in Moschos et al. (2024).

To put these measurements in the context of previous studies of similar systems, we have derived the extinction efficiencies from previous refractive index measurements, since it depends on both particle size and wavelength of incident radiation. Chakrabarty et al. (2010) calculated an average refractive index to be $1.87 + 0.003i$ for spherical BrC and $1.75 + 0.0006i$

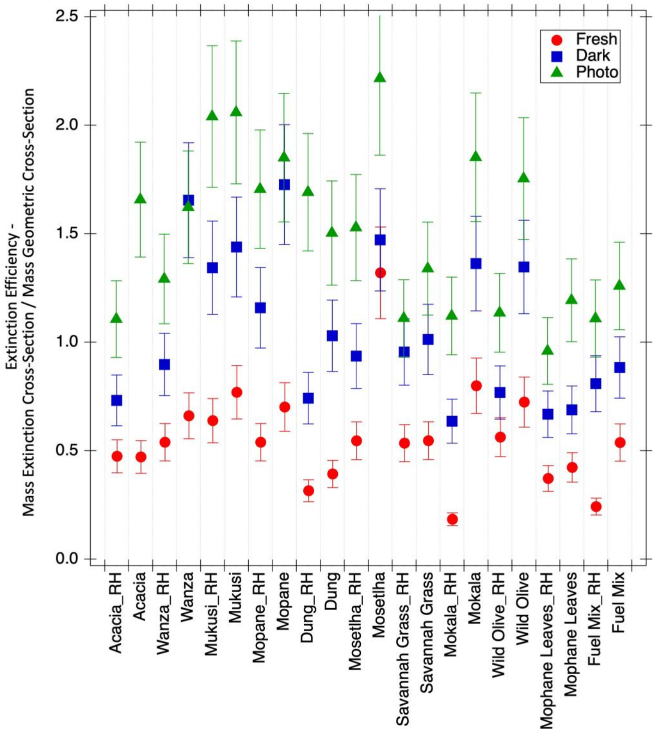

Figure 5. Extinction efficiency measurements for primary fresh, dark aged (without intentional NO_3 radicals added), and photochemical aged BB aerosol for all control experiments.

for Ponderosa Pine Duff BB particles. We used these to calculate the extinction efficiency of 300 nm particles at a wavelength of 550 nm using Mie theory, which was 3.633 for spherical BrC and 3.01 for Ponderosa Pine duff BB aerosol. We used the refractive index of $1.55 + 0.0i$ for non-absorbing organic carbon from Chakrabarty et al. (2010) to calculate an extinction efficiency of 1.44. While the calculated values for spherical BrC and Ponderosa Pine smoke are higher than our values, most likely due to the abundance of BC in the samples that increase the imaginary part of the refractive index, the organic carbon efficiency corresponds well to within our values, especially for aged ones. Additionally, using the average values of the refractive indices from a field study of wild fires by Washenfelder et al. (2013) of 1.634 (±0.004) + 0.021 (±0.005)i, the extinction efficiency calculated was 2.09, which aligns well with our photochemically aged values.

3.4. Impacts of dark aging with NO_3 radicals followed by photochemical aging

In addition to photochemical aging and varying RH, our study considered the impact of nighttime oxidation (added NO_3 radicals) on the aerosol optical properties of African BB emissions (Table S3). Higher MEC and MSC_{Calc} values upon dark aging with added NO_3 radical were observed for most fuels when compared to the MEC and MSC_{Calc} values without the added NO_3 radical. However, a few fuels (i.e., Mukusi and Dung) did not demonstrate any significant change. Note that the NO_3 radicals were formed before smoke emissions were introduced to the chamber, as shown in Figure 2b. While there are studies on the nighttime aging of BrC by NO_3 radicals, they remain limited, resulting in uncertainties within atmospheric models (Jorga et al. 2021; Kodros et al. 2020; 2022; X. Wang et al. 2018).

Although the differences were subtle when comparing the dark aged (without NO_3 radicals intentionally added to the chamber) to the photochemical aged conditions, more significant changes were observed in photochemically aged aerosol that have been previously exposed to NO_3 radicals during the initially dark aging conditions. As shown in Figure 6, in comparing the MEC values from the photochemically aged controls (with prior dark aging without NO_3 radicals added) to photochemically aged experiments that had prior nighttime oxidation conditions with added NO_3 radicals, we found an average difference of $2.5\,m^2\ g^{-1}$. Conversely, photochemically aged MSC_{Calc} measurements in oxidation conditions (with NO_3 added) showed a slightly smaller average difference of $2.4\,m^2\ g^{-1}$ when compared to measurements without oxidants added. Lastly, MAC values from

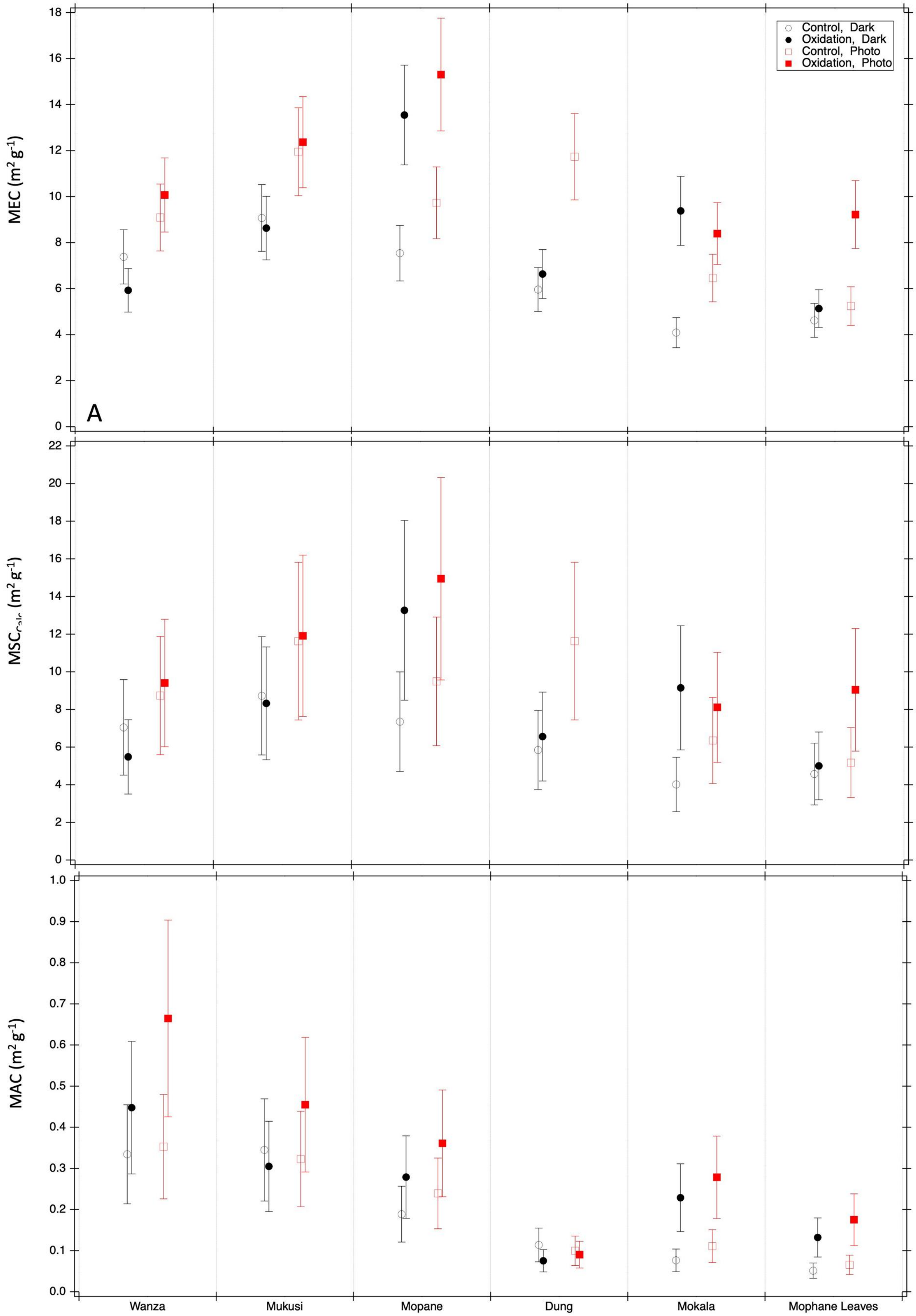

Figure 6. Dark aged and photochemically aged aerosol MEC (a), MSC_{Calc} (b) and MAC (c) in NO_3 radical experiments. The fuels are listed along the x-axis. Note: Control experiments look at the nighttime aging without NO_3 radicals intentionally added followed by photochemical aging, while dark oxidation experiments do the same with the intentional addition of the NO_3 radicals followed by photochemical aging. All these experiments were conducted in humid conditions.

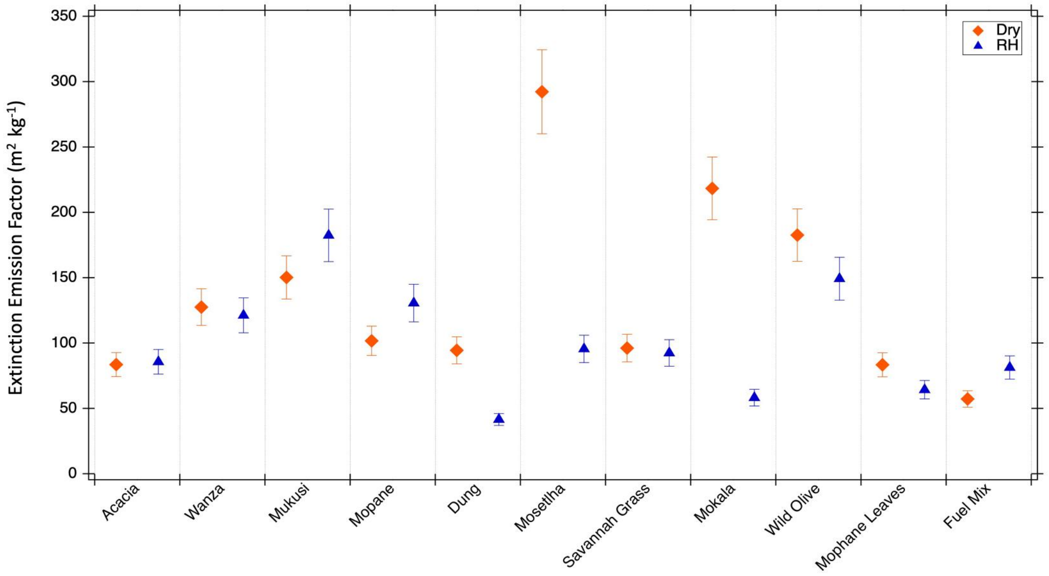

Figure 7. EEF at 550 nm for each fuel during a dry and humid experiment, represented only for fresh emissions.

photochemically aged MAC oxidation measurements had an average difference of 0.1 m^2 g^{-1} when compared to measurements without oxidants added nighttime MEC controls minus MEC nighttime oxidation measurements exhibited an average difference of 1.7 m^2 g^{-1}, while MSC$_{Calc}$ nighttime controls minus MSC$_{Calc}$ nighttime oxidation measurements had an average difference of 1.9 m^2 g^{-1}, and MAC nighttime controls minus oxidation measurements had an average difference of 0.05 m^2 g^{-1}.

3.5. Extinction emission factors

The EEF results reported here are based solely on fresh aerosol emissions under dry (0–10% RH) and humid conditions (65–70% RH) (Figure 7). For the fuels examined under dry conditions, EEFs at 550 nm ranged from 57 ± 6 to 293 ± 32 m^2 kg^{-1}, whereas under humid conditions EEFs ranged from 42 ± 5 to 182 ± 20 m^2 kg^{-1}. Among the fuels tested, three exhibited a statistically significant difference between the values observed under dry and humid conditions. The most statistically significant change was for Mosetlha, where the EEF was nearly 300 ± 33 m^2 kg^{-1} under dry conditions and around 100 ± 11 m^2 kg^{-1} under humid conditions. Additionally, dung and Mokala show similar trends as Mosetlha. The variations in EEFs between dry and humid conditions may be attributed to differences in emission factors specific to each type of fuel (Pokhrel et al. 2021). To our knowledge, there is no study that reported EEF for biomass fuels, but absorption emission factors (AEFs) have been reported (Tian et al. 2019).

3.6. Impact of MCE, RH, dark/photochemical aging, and wavelength of light on SSA

Our initial data reveals an SSA value close to 1, suggesting that the aerosol is dominantly scattering organic compounds in the mid-visible region of the spectrum. The SSA determined using absorption-based methods for smoldering fires is consistent with values in the literature (D. Liu et al. 2014; Pokhrel et al. 2016; Smith et al. 2020), as shown in Figure S3. Our data also showed that humid conditions slightly decreased our SSA values (Figure S4). Specifically, the results reveal an average decrease of 0.006, which, although modest, is noteworthy. This trend suggests that as ambient humidity levels rise, the scattering efficiency of particles diminishes slightly. In contrast, results indicate that photochemical aging tends to increase SSA (Figure S5). On average, there is a 0.002 increase in SSA due to photochemical aging across all fuels. Lastly, our data illustrates neither dark nor photochemical oxidation (with added NO_3 radicals) significantly affects SSA (Figure S6). Except for Wanza where oxidation lowers the SSA by 0.03 under both dark and photochemical aging conditions. Otherwise, there is an average decrease in SSA of 0.004 due to oxidation (with added NO_3 radical). This observation is important because it indicates that the impact of oxidation on SSA varies greatly with different fuel types.

BrC possesses notable light-absorbing characteristics, which can exhibit wavelength-dependent behavior (Kasthuriarachchi et al. 2020; X. Li et al. 2022; Massabò et al. 2015; Pavel et al. 2023; Runa et al. 2022). BrC absorbs significantly at shorter wavelengths

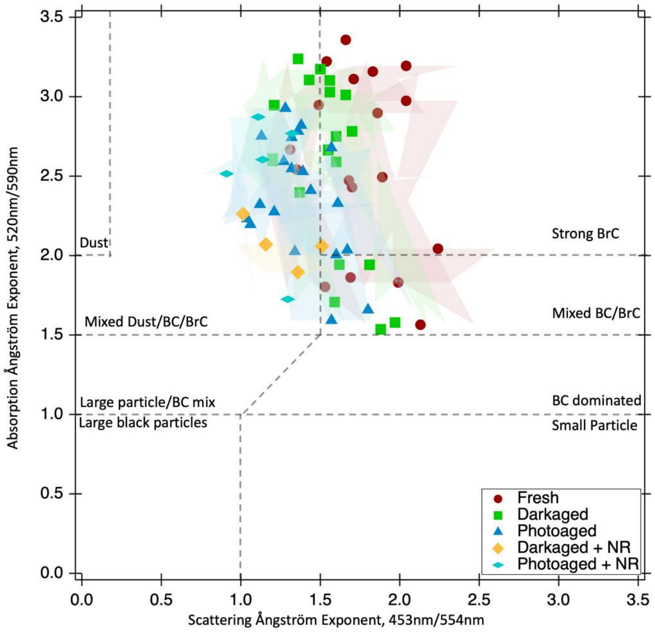

Figure 8. Ångström matrix (i.e., scatter plot of AAE vs SAE). Red circles indicate fresh measurements, green squares indicate dark aged measurements, blue triangles indicate photo aged measurements, and yellow and blue diamonds include the addition of nitrate radical (NR).

(Bond et al. 2013). The observed reduction in SSA at 450 nm in our mostly organic samples suggests heightened absorption by BrC at shorter wavelengths (Kirchstetter, Novakov, and Hobbs 2004). This finding corroborates prior results (Kasthuriarachchi et al. 2020; Lee et al. 2014; X. Li et al. 2022; Massabò et al. 2015; Moschos et al. 2024; Pavel et al. 2023; Runa et al. 2022) emphasizing BrC's significant influence on atmospheric radiative forcing. Our measurements show that we have lower SSA at 450 when compared to 550 nm wavelength measurements (Figure S7). The reduced SSA values observed at 450 nm indicate possible wavelength-dependent behavior of BrC, with absorption contributing more to the extinction at the short vs. long wavelength.

3.7. Wavelength dependence with SAE and AAE

Understanding the wavelength dependence of BrC is imperative for refining climate models and conducting accurate air quality assessments. Previous studies have extensively investigated BrC's role in both regional and global climate dynamics, underscoring its substantial contribution to radiative forcing and its potential implications for temperature and precipitation patterns (Bikkina and Sarin 2019; Bond et al. 2013; Hems et al. 2021; Kirchstetter, Novakov, and Hobbs 2004; Schnitzler et al. 2022)

The SAE verses AAE graphs plots provide valuable insights for identifying the nature and source of aerosols under observation. Figure 8 has the Ångström matrix (i.e., scatter plot of AAE vs SAE) divided to indicate different sources of aerosols. Source labels were derived from (Cazorla et al. 2013). The AAE shows the dependence of absorption on wavelength. BC exhibits an AAE (between 520 nm and 590 nm) of approximately 1, whereas BrC has an AAE exceeding 2 owing to its dependence on the accentuated absorption in the UV (Cappa et al. 2016; Lack and Langridge 2013; C. Liu et al. 2018). SAE (435 nm and 554 nm) shows the dependence of scattering on wavelength. In Figure 8, AAE values range between 1.5 ± 0.24 and 3.3 ± 0.52 under fresh conditions and between 0.7 ± 0.11 and 3.2 ± 0.51 under dark-aged conditions (no NO_3 radical added). The SAE values, on the other hand, show a range of 1.3 ± 0.20 to 2.2 ± 0.35 in fresh conditions and 1.2 ± 0.19 to 1.9 ± 0.30 in dark-aged conditions. For photochemically aged conditions, the AAE values span from 1.5 ± 0.24 to 2.9 ± 0.46, and the SAE values range from 1.0 ± 0.16 to 1.8 ± 0.28. Note: Some points from this figure were unrealistically low due to weak signal and low signal to noise ratio, and therefore removed from the figure.

The range of values for both AAE and SAE decreased upon dark aging and decreased further upon photoaging, as well as with oxidation. This shows that each process reduced the wavelength dependence of scattering and absorption. Cazorla et al. (2013) showed organic-dominated AAE values and SAE values both range from 1.5 to 3. SAE and AAE fall in this same range with a few outliers toward lower SAE values, especially for fresh and dark-aged aerosol (without the added NO_3 radical). This could be due to slight changes in burning conditions (i.e., flaming vs smoldering). Ponczek et al. (2022) conducted aerosol and trace gas sampling in the Amazonian region, with the aerosol composition estimated to be 80–90% organic carbon and the remaining 10–20% comprised of elemental carbon and water-soluble inorganic salts. Their SAEs were determined from the three wavelengths measured with a nephelometer, while AAEs were calculated from the six wavelengths (370–880 nm) using an aethalometer. In Ponczek et al. (2022) the mean value of AAE was 1.8 ± 0.33, reaching a maximum of 3.58. Additionally, the mean value of SAE was 1.67 ± 0.37, with a maximum of 2.31 observed during a substantial wildfire season. These values are consistent with our findings. In a laboratory study using wavelengths of 370–650 nm, Martinsson et al. (2015) found AAE of 2.5–2.7 and estimated the contribution BrC absorption to be 50–70%. L. Zhang, Luo, et al. (2020) found AAE values ranged from 1.17 to 2.92 for six different fuels, which is consistent with our results. Results from C. Liu et al. (2018) showed that BC AAE of fresh emissions were approximately 1.05, and decreased with age to 0.15–0.90. This study showed the same trend with fresh BrC AAE with a median value of 2.52 and decreased with time to a median value of 1.35 for the photoaged measurements.

3.8. Impact on radiative forcing

The effects of humidity, photochemical aging, and NO_3 radical oxidation (in the dark) have resulted in changes in MEC and MSC_{Calc}. To contextualize these cross-sections within a climate framework, we employed Equation (8) based on the change in radiative forcing (ΔF_R) of Chylek and Wong (1995)

$$\frac{\Delta F_{R,1}}{\Delta F_{R,2}} = \frac{\gamma\tau_{scat,1} - \tau_{abs,1}}{\gamma\tau_{scat,2} - \tau_{abs,2}} = \frac{\gamma MSC_1 - MAC_1}{\gamma MSC_2 - MAC_2} \quad (8)$$

Where $\gamma = \frac{(1-R_s)^2\beta}{2R_s}$

Where τ_{scat} and τ_{abs} are the scattering and absorption optical depths, respectfully. R_S is the surface albedo and β is the fraction of the upward-scattered radiation. The scattering and absorption optical depths are the product of path length, mass loading, and mass cross-sections. For our studies path length and mass loading were the same, so this simplifies the equation to the MSC_{Calc} and MAC. To calculate γ we used estimated values of 0.15 for R_S and 0.3 for β (Charlson et al. 1992; Penner et al. 1994), resulting in $\gamma = 0.72$, since we are interested in the average relative change in direct radiative forcing for various conditions. MSC_{Calc} calculations in this work is based off MEC minus MAC measurements.

The decrease in the MEC of fresh emissions due to humid conditions is approximately 0.69, primarily attributed to the change in MSC_{Calc}. Therefore, the cooling effect of fresh BB aerosol decreased by around 0.68 because of humidification. Similarly, photochemically aged BB aerosol under humid conditions experienced a decrease in cooling by a factor of 0.90. Photochemical aging led to an increase in both MAC and MSC_{Calc} by a factor of 1.3–1.7, resulting in a net cooling increase of 1.3 for dry conditions and 1.7 for humid conditions. Oxidation *via* NO_3 radical showed a similar trend, with a cooling increase of 1.3 for both dark- and photochemical aged aerosols. Combining effects, the most significant cooling increase (factor of 2.2) was observed when comparing fresh emissions to those aged in the dark in the presence of NO_3 radical followed by photochemical oxidation under humid conditions.

The Tropospheric Ultraviolet and Visible (TUV) radiation model was also used to estimate the change in spectral irradiance (UCAR 2024). The model was run with a solar zenith angle of 0, a column O_3 of 300 du, and cloudless conditions. The optical depth was 0.4 for each base case, which resulted in a total downwelling of 1.712 to 1.719 $W\ m^{-2} nm^{-1}$, depending on SSA, from 549 to 551 nm. For MEC, the optical depth was scaled for each comparison. Humid conditions result in an average warming of 0.025 and 0.010 $W\ m^{-2}\ nm^{-1}$ for both fresh and primary photochemical aged aerosol (without added NO_3 radical), respectively. Photochemical aging results in an average cooling of 0.031 and 0.065 $W\ m^{-2}\ nm^{-1}$ for aerosols generated under dry and humid conditions, respectively. Finally, the addition of NO_3 radical under humid conditions resulted in a cooling of 0.030 and 0.038 $W\ m^{-2}\ nm^{-1}$ for primary dark and primary photochemically aged aerosol (without added NO_3 radical), respectively.

4. Conclusions

A need for a wider sampling of biomass fuels from other African regions is recommended, since laboratory studies have been focused predominantly on fuels that exist in North American fires (Hodshire et al.

2019). Quantifying trends in emissions from different regions of the world and their impacts on atmospheric composition and chemistry to advance the fundamental atmospheric chemistry knowledge that enables predictive capability for the distribution, reactions, and lifetimes of gases and particles has been a research priority (NAS 2016), and this work focused on Africa contributes to this priority. This present study focused on characterizing the optical and chemical properties of emissions from African biomass fuels collected from sub-Sharan Africa. We explored and quantified how several optical parameters of BBOA particles derived from smoldering-dominated burning of several African biomass fuels with varying aging, humidity, and oxidation (dark and photochemical) conditions.

An accurate estimation of natural and anthropogenic emission inventories is critical for climate and air quality models globally. The lack or scarcity of inventories for African emissions, which are increasing at a dramatic rate due to rapid increase in population and industrialization, may limit the usefulness of current model outputs for development and mitigation strategies for Africa.

We hope this study will provide motivation for further work on African emissions that would help in refining air quality and climate models appropriate for the region. The extensive study of optical properties of BB aerosol emissions from African biomass fuels in this work will help bridge the gap in the available data.

Acknowledgments

We acknowledge Dr. Barbara J. Turpin for invigorating discussions and help editing with the manuscript. We acknowledge Dr. Gizaw Mengistu Tsidu at Botswana International University of Science and Technology for providing the Biomass fuel samples from Botswana. We also acknowledge Kip Carrico and Mercy Ikes for conducting moisture content measurements.

Dedication

This paper dedicated to Professor Solomon Bililign as we celebrate his 72nd birthday. Professor Bililign is a respected scientist and a cherished mentor and advisor. We hope for many more years of his valuable contributions to the field of atmospheric science.

Disclosure statement

No potential conflict of interest was reported by the author(s).

Funding

This work was primarily supported by the United States National Science Foundation (NSF) through the Atmospheric & Geospace Sciences (AGS) Division Grant [# 2100708]. VM acknowledges support by the Swiss National Science Foundation (SNSF) under the Postdoc.Mobility Fellowship grant [P500PN_210745].

ORCID

Megan M. McRee http://orcid.org/0009-0001-8946-2329
Vaios Moschos http://orcid.org/0000-0002-6251-4117
Marc N. Fiddler http://orcid.org/0000-0003-3733-5800
Dario Massabò http://orcid.org/0000-0001-7445-0328
Jason D. Surratt http://orcid.org/0000-0002-6833-1450
Solomon Bililign http://orcid.org/0000-0001-5064-7695

References

Akagi, S. K., R. J. Yokelson, C. Wiedinmyer, M. J. Alvarado, J. S. Reid, T. Karl, J. D. Crounse, and P. O. Wennberg. 2011. Emission factors for open and domestic biomass burning for use in atmospheric models. *Atmos. Chem. Phys.* 11 (9):4039–72. doi: 10.5194/acp-11-4039-2011.

Akinbode, O. M., A. O. Eludoyin, and O. A. Fashae. 2008. Temperature and relative humidity distributions in a medium-size administrative town in southwest Nigeria. *J. Environ. Manage.* 87 (1):95–105. doi: 10.1016/j.jenvman.2007.01.018.

Anderson, T. L., and J. A. Ogren. 1998. Determining aerosol radiative properties using the TSI 3563 integrating nephelometer. *Aerosol Sci. Technol.* 29 (1):57–69. doi: 10.1080/02786829808965551.

Andreae, M. O. 2019. Emission of trace gases and aerosols from biomass burning – An updated assessment. *Atmos. Chem. Phys.* 19 (13):8523–46. doi: 10.5194/acp-19-8523-2019.

Beyene, A. D., and S. F. Koch. 2013. Clean fuel-saving technology adoption in urban Ethiopia. *Energy Econ.* 36:605–13. doi: 10.1016/j.eneco.2012.11.003.

Bikkina, S., and M. Sarin. 2019. Brown carbon in the continental outflow to the North Indian Ocean. *Environ. Sci. Process. Impacts.* 21 (6):970–87. doi: 10.1039/C9EM00089E.

Bluvshtein, N., P. Lin, J. M. Flores, L. Segev, Y. Mazar, E. Tas, G. Snider, C. Weagle, S. S. Brown, A. Laskin, et al. 2017. Broadband optical properties of biomass-burning aerosol and identification of brown carbon chromophores. *JGR. Atmospheres* 122 (10):5441–56. doi: 10.1002/2016JD026230.

Bond, T. C., S. J. Doherty, D. W. Fahey, P. M. Forster, T. Berntsen, B. J. DeAngelo, M. G. Flanner, S. Ghan, B. Kärcher, D. Koch, et al. 2013. Bounding the role of black carbon in the climate system: A scientific assessment. *JGR. Atmospheres* 118 (11):5380–552. doi: 10.1002/jgrd.50171.

Brock, C. A., N. L. Wagner, B. E. Anderson, A. R. Attwood, A. Beyersdorf, P. Campuzano-Jost, A. G. Carlton, D. A. Day, G. S. Diskin, T. D. Gordon, et al. 2016. Aerosol optical properties in the southeastern United States in summer – Part 1: Hygroscopic growth. *Atmos. Chem. Phys.* 16 (8):4987–5007. doi: 10.5194/acp-16-4987-2016.

Brown, H., X. Liu, R. Pokhrel, S. Murphy, Z. Lu, R. Saleh, T. Mielonen, H. Kokkola, T. Bergman, G. Myhre, et al. 2021. Biomass burning aerosols in most climate models are too absorbing. *Nat. Commun.* 12 (1):277. doi: 10.1038/s41467-020-20482-9.

Browne, E. C., X. Zhang, J. P. Franklin, K. J. Ridley, T. W. Kirchstetter, K. R. Wilson, C. D. Cappa, and J. H. Kroll. 2019. Effect of heterogeneous oxidative aging on light absorption by biomass burning organic aerosol. *Aerosol Sci. Technol.* 53 (6):663–74. doi: 10.1080/02786826.2019.1599321.

Cappa, C. D., K. R. Kolesar, X. Zhang, D. B. Atkinson, M. S. Pekour, R. A. Zaveri, A. Zelenyuk, and Q. Zhang. 2016. Understanding the optical properties of ambient sub- and supermicron particulate matter: Results from the CARES 2010 field study in northern California. *Atmos. Chem. Phys.* 16 (10):6511–35. doi: 10.5194/acp-16-6511-2016.

Cazorla, A., R. Bahadur, K. J. Suski, J. F. Cahill, D. Chand, B. Schmid, V. Ramanathan, and K. A. Prather. 2013. Relating aerosol absorption due to soot, organic carbon, and dust to emission sources determined from in-situ chemical measurements. *Atmos. Chem. Phys.* 13 (18):9337–50. doi: 10.5194/acp-13-9337-2013.

Cecchini, M. A., L. A. T. Machado, M. O. Andreae, S. T. Martin, R. I. Albrecht, P. Artaxo, H. M. J. Barbosa, S. Borrmann, D. Fütterer, T. Jurkat, et al. 2017. Sensitivities of Amazonian clouds to aerosols and updraft speed. *Atmos. Chem. Phys.* 17 (16):10037–50. doi: 10.5194/acp-17-10037-2017.

Chakrabarty, R. K., H. Moosmüller, L. W. A. Chen, K. Lewis, W. P. Arnott, C. Mazzoleni, M. K. Dubey, C. E. Wold, W. M. Hao, and S. M. Kreidenweis. 2010. Brown carbon in tar balls from smoldering biomass combustion. *Atmos. Chem. Phys.* 10 (13):6363–70. doi: 10.5194/acp-10-6363-2010.

Charlson, R. J., S. E. Schwartz, J. M. Hales, R. D. Cess, J. A. Coakley, J. E. Hansen, and D. J. Hofmann. 1992. Climate forcing by anthropogenic aerosols. *Science* 255 (5043):423–30. doi: 10.1126/science.255.5043.423.

Chen, Y., and T. C. Bond. 2010. Light absorption by organic carbon from wood combustion. *Atmos. Chem. Phys.* 10 (4):1773–87. doi: 10.5194/acp-10-1773-2010.

Cheng, Y. F., A. Wiedensohler, H. Eichler, J. Heintzenberg, M. Tesche, A. Ansmann, M. Wendisch, H. Su, D. Althausen, H. Herrmann, et al. 2008. Relative humidity dependence of aerosol optical properties and direct radiative forcing in the surface boundary layer at Xinken in Pearl River Delta of China: An observation based numerical study. *Atmos. Environ.* 42 (25):6373–97. doi: 10.1016/j.atmosenv.2008.04.009.

Chylek, P., and J. Wong. 1995. Effect of absorbing aerosols on global radiation budget. *Geophys. Res. Lett.* 22 (8):929–31. doi: 10.1029/95GL00800.

Crutzen, P. J., and M. O. Andreae. 1990. Biomass burning in the tropics: Impact on atmospheric chemistry and biogeochemical cycles. *Science* 250 (4988):1669–78. doi: 10.1126/science.250.4988.1669.

Crutzen, P. J., and M. O. Andreae. 2016. Biomass burning in the tropics: Impact on atmospheric chemistry and biogeochemical cycles. In *Paul J. Crutzen: A Pioneer on Atmospheric Chemistry and Climate Change in the Anthropocene*, ed. J. P. Crutzen and G. H. Brauch. Cham: Springer International Publishing.

Evangeliou, N., A. Kylling, S. Eckhardt, V. Myroniuk, K. Stebel, R. Paugam, S. Zibtsev, and A. Stohl. 2019. Open fires in Greenland in summer 2017: Transport, deposition and radiative effects of BC, OC and BrC emissions. *Atmos. Chem. Phys.* 19 (2):1393–411. doi: 10.5194/acp-19-1393-2019.

Feng, Y., V. Ramanathan, and V. R. Kotamarthi. 2013. Brown carbon: A significant atmospheric absorber of solar radiation? *Atmos. Chem. Phys.* 13 (17):8607–21. doi: 10.5194/acp-13-8607-2013.

Flores, J. M., R. Z. Bar-Or, N. Bluvshtein, A. Abo-Riziq, A. Kostinski, S. Borrmann, I. Koren, I. Koren, and Y. Rudich. 2012. Absorbing aerosols at high relative humidity: Linking hygroscopic growth to optical properties. *Atmos. Chem. Phys.* 12 (12):5511–21. doi: 10.5194/acp-12-5511-2012.

Fry, J. L., A. Kiendler-Scharr, A. W. Rollins, T. Brauers, S. S. Brown, H. P. Dorn, W. P. Dubé, H. Fuchs, A. Mensah, F. Rohrer, et al. 2011. SOA from limonene: Role of NO_3 in its generation and degradation. *Atmos. Chem. Phys.* 11 (8):3879–94. doi: 10.5194/acp-11-3879-2011.

Hamilton, D. S., S. Hantson, C. E. Scott, J. O. Kaplan, K. J. Pringle, L. P. Nieradzik, A. Rap, G. A. Folberth, D. V. Spracklen, and K. S. Carslaw. 2018. Reassessment of pre-industrial fire emissions strongly affects anthropogenic aerosol forcing. *Nat. Commun.* 9 (1):3182. doi: 10.1038/s41467-018-05592-9.

Hamilton, J. F., D. J. Bryant, P. M. Edwards, B. Ouyang, T. J. Bannan, A. Mehra, A. W. Mayhew, J. R. Hopkins, R. E. Dunmore, F. A. Squires, et al. 2021. Key role of NO(3) radicals in the production of isoprene nitrates and nitrooxyorganosulfates in Beijing. *Environ. Sci. Technol.* 55 (2):842–53. doi: 10.1021/acs.est.0c05689.

Hand, J. L., and W. C. Malm. 2007. Review of aerosol mass scattering efficiencies from ground-based measurements since 1990. *J. Geophys. Res.* 112 (D16):D16203. doi: 10.1029/2007JD008484.

Health Effects Institute. 2020. *State of global air 2020*. Boston, MA: Health Effects Institute.

Hems, R. F., and J. P. D. Abbatt. 2018. Aqueous phase photo-oxidation of brown carbon nitrophenols: Reaction kinetics, mechanism, and evolution of light absorption. *ACS Earth Space Chem.* 2 (3):225–34. doi: 10.1021/acsearthspacechem.7b00123.

Hems, R. F., E. G. Schnitzler, C. Liu-Kang, C. D. Cappa, and J. P. D. Abbatt. 2021. Aging of atmospheric brown carbon aerosol. *ACS Earth Space Chem.* 5 (4):722–48. doi: 10.1021/acsearthspacechem.0c00346.

Hodshire, A. L., A. Akherati, M. J. Alvarado, B. Brown-Steiner, S. H. Jathar, J. L. Jimenez, S. M. Kreidenweis, C. R. Lonsdale, T. B. Onasch, A. M. Ortega, et al. 2019. Aging effects on biomass burning aerosol mass and composition: A critical review of field and laboratory studies. *Environ. Sci. Technol.* 53 (17):10007–22. doi: 10.1021/acs.est.9b02588.

Ichoku, C. 2020. *African Biomass Burning and Its Atmospheric Impacts*. Oxford: Oxford University Press.

Ichoku, C., L. T. Ellison, K. Elena Willmot, T. Matsui, A. K. Dezfuli, C. K. Gatebe, J. Wang, E. M. Wilcox, J. Lee, J. Adegoke, et al. 2016. Biomass burning, land-cover change, and the hydrological cycle in Northern sub-Saharan Africa. *Environ. Res. Lett.* 11 (9):095005. doi: 10.1088/1748-9326/11/9/095005.

Jacobson, M. Z. 2014. Effects of biomass burning on climate, accounting for heat and moisture fluxes, black and brown carbon, and cloud absorption effects. *JGR. Atmospheres* 119 (14):8980–9002. doi: 10.1002/2014JD021861.

Jain, N., A. Le Moine, G. Chaussonnet, A. Flatau, L. Bravo, A. Ghoshal, M. J. Walock, M. Murugan, and P. Khare. 2021. A critical review of physical models in high temperature multiphase fluid dynamics: Turbulent transport and particle-wall interactions. *Applied Mechanics Reviews* 73 (4):040801. doi: 10.1115/1.4051503.

Jianhua, C. H. E. N., S. H. E. N. Yicheng, C. H. I. Xiangyu, and Z. H. U. Shuang. 2023. Factors influencing the hygroscopicity of aerosols and the effects of hygroscopicity on aerosol optical properties. *- Journal of Environmental Engineering Technology* 13 (6):2081. doi: 10.12153/j.issn.1674-991X.20230052.

Jin, X., Z. Li, T. Wu, Y. Wang, Y. Cheng, T. Su, J. Wei, R. Ren, H. Wu, S. Li, et al. 2022. The different sensitivities of aerosol optical properties to particle concentration, humidity, and hygroscopicity between the surface level and the upper boundary layer in Guangzhou, China. *Sci. Total Environ.* 803:150010. doi: 10.1016/j.scitotenv.2021.150010.

Jolleys, M. D., H. Coe, G. McFiggans, G. Capes, J. D. Allan, J. Crosier, P. I. Williams, G. Allen, K. N. Bower, J. L. Jimenez, et al. 2012. Characterizing the aging of biomass burning organic aerosol by use of mixing ratios: A meta-analysis of four regions. *Environ. Sci. Technol.* 46 (24):13093–102. doi: 10.1021/es302386v.

Jorga, S. D., K. Florou, C. Kaltsonoudis, J. K. Kodros, C. Vasilakopoulou, M. Cirtog, A. Fouqueau, B. Picquet-Varrault, A. Nenes, and S. N. Pandis. 2021. Nighttime chemistry of biomass burning emissions in urban areas: A dual mobile chamber study. *Atmos. Chem. Phys.* 21 (19):15337–49. doi: 10.5194/acp-21-15337-2021.

Kasthuriarachchi, N. Y., L.-H. Rivellini, M. G. Adam, and A. K. Y. Lee. 2020. Light absorbing properties of primary and secondary brown carbon in a tropical urban environment. *Environ. Sci. Technol.* 54 (17):10808–19. doi: 10.1021/acs.est.0c02414.

Kirchstetter, T. W., T. Novakov, and P. V. Hobbs. 2004. Evidence that the spectral dependence of light absorption by aerosols is affected by organic carbon. *J. Geophys. Res.* 109 (D21):D21208. doi: 10.1029/2004JD004999.

Kleinman, L. I., A. J. Sedlacek Iii, K. Adachi, P. R. Buseck, S. Collier, M. K. Dubey, A. L. Hodshire, E. Lewis, T. B. Onasch, J. R. Pierce, et al. 2020. Rapid evolution of aerosol particles and their optical properties downwind of wildfires in the western US. *Atmos. Chem. Phys.* 20 (21):13319–41. doi: 10.5194/acp-20-13319-2020.

Kodros, J. K., C. Kaltsonoudis, M. Paglione, K. Florou, S. Jorga, C. Vasilakopoulou, M. Cirtog, M. Cazaunau, B. Picquet-Varrault, A. Nenes, et al. 2022. Secondary aerosol formation during the dark oxidation of residential biomass burning emissions. *Environ. Sci. Atmos.* 2 (5):1221–36. doi: 10.1039/D2EA00031H.

Kodros, J. K., D. K. Papanastasiou, M. Paglione, M. Masiol, S. Squizzato, K. Florou, K. Skyllakou, C. Kaltsonoudis, A. Nenes, and S. N. Pandis. 2020. Rapid dark aging of biomass burning as an overlooked source of oxidized organic aerosol. *Proc. Natl. Acad. Sci. U S A* 117 (52):33028–33. doi: 10.1073/pnas.2010365117.

Kondo, Y., H. Matsui, N. Moteki, L. Sahu, N. Takegawa, M. Kajino, Y. Zhao, M. J. Cubison, J. L. Jimenez, S. Vay, et al. 2011. Emissions of black carbon, organic, and inorganic aerosols from biomass burning in North America and Asia in 2008. *J. Geophys. Res.* 116 (D8):D08204. doi: 10.1029/2010JD015152.

Konovalov, I. B., N. A. Golovushkin, M. Beekmann, and M. O. Andreae. 2021. Insights into the aging of biomass burning aerosol from satellite observations and 3D atmospheric modeling: Evolution of the aerosol optical properties in Siberian wildfire plumes. *Atmos. Chem. Phys.* 21 (1):357–92. doi: 10.5194/acp-21-357-2021.

Koop, T., J. Bookhold, M. Shiraiwa, and U. Pöschl. 2011. Glass transition and phase state of organic compounds: Dependency on molecular properties and implications for secondary organic aerosols in the atmosphere. *Phys. Chem. Chem. Phys.* 13 (43):19238–55. doi: 10.1039/C1CP22617G.

Kroll, J. H., C. Y. Lim, S. H. Kessler, and K. R. Wilson. 2015. Heterogeneous oxidation of atmospheric organic aerosol: Kinetics of changes to the amount and oxidation state of particle-phase organic carbon. *J. Phys. Chem. A* 119 (44):10767–83. doi: 10.1021/acs.jpca.5b06946.

Lack, D. A., and J. M. Langridge. 2013. On the attribution of black and brown carbon light absorption using the Ångström exponent. *Atmos. Chem. Phys.* 13 (20):10535–43. doi: 10.5194/acp-13-10535-2013.

Laris, P., M. Koné, F. Dembélé, C. M. Rodrigue, L. Yang, R. Jacobs, and Q. Laris. 2021. Methane gas emissions from savanna fires: What analysis of local burning regimes in a working West African landscape tell us. *Biogeosciences* 18 (23):6229–44. doi: 10.5194/bg-18-6229-2021.

Lavi, A., P. Lin, B. Bhaduri, R. Carmieli, A. Laskin, and Y. Rudich. 2017. Characterization of light-absorbing oligomers from reactions of phenolic compounds and Fe(III). *ACS Earth Space Chem.* 1 (10):637–46. doi: 10.1021/acsearthspacechem.7b00099.

Lee, H., S.-J. Jeong, O. Kalashnikova, M. Tosca, S.-W. Kim, and J.-S. Kug. 2018. Characterization of wildfire-induced aerosol emissions from the maritime continent peatland and central african dry savannah with MISR and CALIPSO aerosol products. *JGR. Atmospheres* 123 (6):3116–25. doi: 10.1002/2017JD027415.

Lee, H. J., P. K. Aiona, A. Laskin, J. Laskin, and S. A. Nizkorodov. 2014. Effect of solar radiation on the optical properties and molecular composition of laboratory proxies of atmospheric brown carbon. *Environ. Sci. Technol.* 48 (17):10217–26. doi: 10.1021/es502515r.

Leskinen, J., A. Hartikainen, S. Väätäinen, M. Ihalainen, A. Virkkula, A. Mesceriakovas, P. Tiitta, M. Miettinen, H. Lamberg, H. Czech, et al. 2023. Photochemical aging induces changes in the effective densities, morphologies, and optical properties of combustion aerosol particles.

Environ. Sci. Technol. 57 (13):5137–48. doi: 10.1021/acs.est.2c04151.

Li, C., Q. He, J. Schade, J. Passig, R. Zimmermann, D. Meidan, A. Laskin, and Y. Rudich. 2019. Dynamic changes in optical and chemical properties of tar ball aerosols by atmospheric photochemical aging. *Atmos. Chem. Phys.* 19 (1):139–63. doi: 10.5194/acp-19-139-2019.

Li, C., Y. Hu, J. Chen, Z. Ma, X. Ye, X. Yang, L. Wang, X. Wang, and A. Mellouki. 2016. Physiochemical properties of carbonaceous aerosol from agricultural residue burning: Density, volatility, and hygroscopicity. *Atmos. Environ.* 140:94–105. doi: 10.1016/j.atmosenv.2016.05.052.

Li, C. L., Z. Ma, J. M. Chen, X. M. Wang, X. N. Ye, L. Wang, X. Yang, H. D. Kan, D. J. Donaldson, and A. Mellouki. 2015. Evolution of biomass burning smoke particles in the dark. *Atmos. Environ.* 120:244–52. doi: 10.1016/j.atmosenv.2015.09.003.

Li, C., Q. He, Z. Fang, S. S. Brown, A. Laskin, S. R. Cohen, and Y. Rudich. 2020. Laboratory insights into the diel cycle of optical and chemical transformations of biomass burning brown carbon aerosols. *Environ. Sci. Technol.* 54 (19):11827–37. doi: 10.1021/acs.est.0c04310.

Li, X., N. Sun, Q. Jin, Z. Zhao, L. Wang, Q. Wang, X. Gu, Y. Li, and X. Liu. 2022. Light absorption properties of black and brown carbon in winter over the North China Plain: Impacts of regional biomass burning. *Atmos. Environ.* 278:119100. doi: 10.1016/j.atmosenv.2022.119100.

Lin, G., J. E. Penner, M. G. Flanner, S. Sillman, L. Xu, and C. Zhou. 2014. Radiative forcing of organic aerosol in the atmosphere and on snow: Effects of SOA and brown carbon. *J. Geophys. Res. Atmos.* 119 (12):7453–76. doi: 10.1002/2013JD021186.

Liu, C., C. E. Chung, Y. Yin, and M. Schnaiter. 2018. The absorption Ångström exponent of black carbon: From numerical aspects. *Atmos. Chem. Phys.* 18 (9):6259–73. doi: 10.5194/acp-18-6259-2018.

Liu, D., J. D. Allan, D. E. Young, H. Coe, D. Beddows, Z. L. Fleming, M. J. Flynn, M. W. Gallagher, R. M. Harrison, J. Lee, et al. 2014. Size distribution, mixing state and source apportionment of black carbon aerosol in London during wintertime. *Atmos. Chem. Phys.* 14 (18):10061–84. doi: 10.5194/acp-14-10061-2014.

Liu, J., P. Lin, A. Laskin, J. Laskin, S. M. Kathmann, M. Wise, R. Caylor, F. Imholt, V. Selimovic, and J. E. Shilling. 2016. Optical properties and aging of light-absorbing secondary organic aerosol. *Atmos. Chem. Phys.* 16 (19):12815–27. doi: 10.5194/acp-16-12815-2016.

Liu, Q., D. Liu, Q. Gao, P. Tian, F. Wang, D. Zhao, K. Bi, Y. Wu, S. Ding, K. Hu, et al. 2020. Vertical characteristics of aerosol hygroscopicity and impacts on optical properties over the North China Plain during winter. *Atmos. Chem. Phys.* 20 (6):3931–44. doi: 10.5194/acp-20-3931-2020.

Liu, X., Y. Cheng, Y. Zhang, J. Jung, N. Sugimoto, S.-Y. Chang, Y. J. Kim, S. Fan, and L. Zeng. 2008. Influences of relative humidity and particle chemical composition on aerosol scattering properties during the 2006 PRD campaign. *Atmos. Environ.* 42 (7):1525–36. doi: 10.1016/j.atmosenv.2007.10.077.

Lu, Z., D. G. Streets, E. Winijkul, F. Yan, Y. Chen, T. C. Bond, Y. Feng, M. K. Dubey, S. Liu, J. P. Pinto, et al. 2015. Light absorption properties and radiative effects of primary organic aerosol emissions. *Environ. Sci. Technol.* 49 (8):4868–77. doi: 10.1021/acs.est.5b00211.

Magee Scientific. 2016. *Aethalometer Model AE33 user manual*. Ljubljana: Magee Scientific.

Magi, B. I., and P. V. Hobbs. 2003. Effects of humidity on aerosols in southern Africa during the biomass burning season. *J. Geophys. Res.* 108 (D13):8495. doi: 10.1029/2002JD002144.

Marsavin, A., R. van Gageldonk, N. Bernays, N. W. May, D. A. Jaffe, and J. L. Fry. 2023. Optical properties of biomass burning aerosol during the 2021 Oregon fire season: Comparison between wild and prescribed fires. *Environ. Sci: Atmos.* 3 (3):608–26. doi: 10.1039/D2EA00118G.

Martinsson, J., A. C. Eriksson, I. E. Nielsen, V. Berg Malmborg, E. Ahlberg, C. Andersen, R. Lindgren, R. Nyström, E. Z. Nordin, W. H. Brune, et al. 2015. Impacts of combustion conditions and photochemical processing on the light absorption of biomass combustion aerosol. *Environ. Sci. Technol.* 49 (24):14663–71. doi: 10.1021/acs.est.5b03205.

Massabò, D., V. Bernardoni, M. C. Bove, A. Brunengo, E. Cuccia, A. Piazzalunga, P. Prati, G. Valli, and R. Vecchi. 2013. A multi-wavelength optical set-up for the characterization of carbonaceous particulate matter. *J. Aerosol Sci.* 60:34–46. doi: 10.1016/j.jaerosci.2013.02.006.

Massabò, D., L. Caponi, V. Bernardoni, M. C. Bove, P. Brotto, G. Calzolai, F. Cassola, M. Chiari, M. E. Fedi, P. Fermo, et al. 2015. Multi-wavelength optical determination of black and brown carbon in atmospheric aerosols. *Atmos. Environ.* 108:1–12. doi: 10.1016/j.atmosenv.2015.02.058.

McMeeking, G. R., S. M. Kreidenweis, S. Baker, C. M. Carrico, J. C. Chow, J. L. Collett, Jr., W. M. Hao, A. S. Holden, T. W. Kirchstetter, W. C. Malm, et al. 2009. Emissions of trace gases and aerosols during the open combustion of biomass in the laboratory. *J. Geophys. Res.* 114 (D19):D19210. doi: 10.1029/2009JD011836.

Moosmüller, H., R. Varma, and W. P. Arnott. 2005. Cavity ring-down and cavity-enhanced detection techniques for the measurement of aerosol extinction. *Aerosol Sci. Technol.* 39 (1):30–9. doi: 10.1080/027868290903880.

Moschos, V., N. K. Kumar, K. R. Daellenbach, U. Baltensperger, A. S. H. Prévôt, and I. El Haddad. 2018. Source apportionment of brown carbon absorption by coupling ultraviolet–visible spectroscopy with aerosol mass spectrometry. *Environ. Sci. Technol. Lett.* 5 (6):302–8. doi: 10.1021/acs.estlett.8b00118.

Moschos, V., C. Christensen, M. Mouton, M. Fiddler, T. Isolabella, F. Mazzei, D. Massabò, B. J. Turpin, S. Bililign, and J. Surratt. 2024. Quantifying the light-absorption properties and molecular composition of brown carbon aerosol from Sub-Saharan African biomass combustion. *Environ. Sci. Technol.* 58 (9):4268–80. doi: 10.1021/acs.est.3c09378.

Moschos, V., M. Gysel-Beer, R. L. Modini, J. C. Corbin, D. Massabò, C. Costa, S. G. Danelli, A. Vlachou, K. R. Daellenbach, S. Szidat, et al. 2021. Source-specific light absorption by carbonaceous components in the complex aerosol matrix from yearly filter-based measurements. *Atmos. Chem. Phys.* 21 (17):12809–33. doi: 10.5194/acp-21-12809-2021.

Moschos, V. 2021. *Assessing the composition and sources of climate-relevant atmospheric aerosol species*. Zurich: ETH Zurich.

Mouton, M., K. A. Malek, M. H. James, R. P. Pokhrel, M. N. Fiddler, A. A. Asa-Awuku, and S. Bililign. 2023. The hygroscopic properties of biomass burning aerosol from Eucalyptus and cow dung under different combustion conditions. *Aerosol Sci. Technol.* 57 (7):665–77. doi: 10.1080/02786826.2023.2198587.

NAS. 2016. *The future of atmospheric chemistry research: Remembering yesterday, understanding today, anticipating tomorrow*. Washington, DC: National Academy of Sciences.

Paulson, S. E., P. J. Gallimore, X. M. Kuang, J. R. Chen, M. Kalberer, and D. H. Gonzalez. 2019. A light-driven burst of hydroxyl radicals dominates oxidation chemistry in newly activated cloud droplets. *Sci. Adv.* 5 (5):eaav7689. doi: 10.1126/sciadv.aav7689.

Pavel, M. R. S., S. U. Zaman, S. Paul, P. Zaman, and A. Salam. 2023. Light absorption properties of black carbon and brown carbon emitted from biomass combustion at the typical rural cooking stoves in Bangladesh. *Air Qual. Atmos. Health* 16 (4):719–32. doi: 10.1007/s11869-023-01302-7.

Penner, J. E., R. J. Charlson, J. M. Hales, N. S. Laulainen, R. Leifer, T. Novakov, J. Ogren, L. F. Radke, S. E. Schwartz, and L. Travis. 1994. Quantifying and minimizing uncertainty of climate forcing by anthropogenic aerosols. *Bull. Amer. Meteor. Soc.* 75 (3):375–400. doi: 10.1175/1520-0477(1994)075<0375:QAMUOC>2.0.CO;2.

Pokhrel, R. P., J. Gordon, M. N. Fiddler, and S. Bililign. 2020. Impact of combustion conditions on physical and morphological properties of biomass burning aerosol. *Aerosol Sci. Technol.* 55 (1):80–91. doi: 10.1080/02786826.2020.1822512.

Pokhrel, R. P., J. Gordon, M. N. Fiddler, and S. Bililign. 2021. Determination of emission factors of pollutants from biomass burning of African fuels in laboratory measurements. *JGR. Atmospheres* 126 (20): e2021JD034731. doi: 10.1029/2021JD034731.

Pokhrel, R. P., N. L. Wagner, J. M. Langridge, D. A. Lack, T. Jayarathne, E. A. Stone, C. E. Stockwell, R. J. Yokelson, and S. M. Murphy. 2016. Parameterization of single-scattering albedo (SSA) and absorption Ångström exponent (AAE) with EC / OC for aerosol emissions from biomass burning. *Atmos. Chem. Phys.* 16 (15):9549–61. doi: 10.5194/acp-16-9549-2016.

Ponczek, M., M. Franco, S. Carbone, L. Rizzo, D. Monteiro dos Santos, F. Morais, A. Duarte, H. Barbosa, and P. Artaxo. 2022. Linking chemical composition and optical properties of biomass burning aerosols in Amazonia. *Environmental Science: Atmospheres*. (2):252–69. doi: 10.1039/D1EA00055A.

Ramo, R., E. Roteta, I. Bistinas, D. van Wees, A. Bastarrika, E. Chuvieco, and G. R. van der Werf. 2021. African burned area and fire carbon emissions are strongly impacted by small fires undetected by coarse resolution satellite data. *Proc. Natl. Acad. Sci. USA.* 118 (9): e2011160118. doi: 10.1073/pnas.2011160118.

Rollins, A. W., A. Kiendler-Scharr, J. L. Fry, T. Brauers, S. S. Brown, H. P. Dorn, W. P. Dubé, H. Fuchs, A. Mensah, T. F. Mentel, et al. 2009. Isoprene oxidation by nitrate radical: Alkyl nitrate and secondary organic aerosol yields. *Atmos. Chem. Phys.* 9 (18):6685–703. doi: 10.5194/acp-9-6685-2009.

Runa, F., M. S. Islam, F. Jeba, and A. Salam. 2022. Light absorption properties of brown carbon from biomass burning emissions. *Environ. Sci. Pollut. Res. Int.* 29 (14): 21012–22. doi: 10.1007/s11356-021-17220-z.

Saleh, R., Z. Cheng, and K. Atwi. 2018. The Brown–Black continuum of light-absorbing combustion aerosols. *Environ. Sci. Technol. Lett.* 5 (8):508–13. doi: 10.1021/acs.estlett.8b00305.

Santos, F., K. Longo, A. Guenther, S. Kim, D. Gu, D. Oram, G. Forster, J. Lee, J. Hopkins, J. Brito, et al. 2018. Biomass burning emission disturbances of isoprene oxidation in a tropical forest. *Atmos. Chem. Phys.* 18 (17): 12715–34. doi: 10.5194/acp-18-12715-2018.

Schnitzler, E. G., N. G. A. Gerrebos, T. S. Carter, Y. Huang, C. L. Heald, A. K. Bertram, and J. P. D. Abbatt. 2022. Rate of atmospheric brown carbon whitening governed by environmental conditions. *Proc. Natl. Acad. Sci. U S A* 119 (38):e2205610119. doi: 10.1073/pnas.2205610119.

Shilling, J. E., M. A. Zawadowicz, J. Liu, R. A. Zaveri, and A. Zelenyuk. 2019. Photochemical aging alters secondary organic aerosol partitioning behavior. *ACS Earth Space Chem.* 3 (12):2704–16. doi: 10.1021/acsearthspacechem.9b00248.

Singh, S., M. N. Fiddler, and S. Bililign. 2016. Measurement of size-dependent single scattering albedo of fresh biomass burning aerosols using the extinction-minus-scattering technique with a combination of cavity ring-down spectroscopy and nephelometry. *Atmos. Chem. Phys.* 16 (21):13491–507. doi: 10.5194/acp-16-13491-2016.

Singh, S., M. N. Fiddler, D. Smith, and S. Bililign. 2014. Error analysis and uncertainty in the determination of aerosol optical properties using cavity ring-down spectroscopy, integrating nephelometry, and the extinction-minus-scattering method. *Aerosol Sci. Technol.* 48 (12): 1345–59. doi: 10.1080/02786826.2014.984062.

Smith, D. M., M. N. Fiddler, R. P. Pokhrel, and S. Bililign. 2020. Laboratory studies of fresh and aged biomass burning aerosol emitted from east African biomass fuels – Part 1: Optical properties. *Atmos. Chem. Phys.* 20 (17): 10149–68. doi: 10.5194/acp-20-10149-2020.

Smith, D. M., M. N. Fiddler, K. G. Sexton, and S. Bililign. 2019. Construction and characterization of an indoor smog chamber for measuring the optical and physicochemical properties of aging biomass burning aerosols. *Aerosol Air Qual. Res.* 19 (3):467–83. doi: 10.4209/aaqr.2018.06.0243.

Strawa, A. W., R. Elleman, A. G. Hallar, D. Covert, K. Ricci, R. Provencal, T. W. Owano, H. H. Jonsson, B. Schmid, A. P. Luu, et al. 2006. Comparison of in situ aerosol extinction and scattering coefficient measurements made during the Aerosol Intensive Operating Period. *J. Geophys. Res.* 111 (D5):D05s03. doi: 10.1029/2005JD006056.

Sumlin, B. J., A. Pandey, M. J. Walker, R. S. Pattison, B. J. Williams, and R. K. Chakrabarty. 2017. Atmospheric photooxidation diminishes light absorption by primary brown carbon aerosol from biomass burning. *Environ. Sci. Technol. Lett.* 4 (12):540–5. doi: 10.1021/acs.estlett.7b00393.

Surratt, J. D., Y. Gómez-González, A. W. Chan, R. Vermeylen, M. Shahgholi, T. E. Kleindienst, E. O. Edney, J. H. Offenberg, M. Lewandowski, M. Jaoui, et al. 2008. Organosulfate formation in biogenic secondary organic aerosol. *J. Phys. Chem. A* 112 (36):8345–78. doi: 10.1021/jp802310p.

Thompson, J. E., N. Barta, D. Policarpio, and R. DuVall. 2008. A fixed frequency aerosol albedometer. *Opt. Express.* 16 (3):2191–205. doi: 10.1364/Oe.16.002191.

Thompson, J. E., B. W. Smith, and J. D. Winefordner. 2002. Monitoring atmospheric particulate matter through cavity ring-down spectroscopy. *Anal. Chem.* 74 (9):1962–7. doi: 10.1021/ac0110505.

Thornhill, G. D., C. L. Ryder, E. J. Highwood, L. C. Shaffrey, and B. T. Johnson. 2018. The effect of South American biomass burning aerosol emissions on the regional climate. *Atmos. Chem. Phys.* 18 (8):5321–42. doi: 10.5194/acp-18-5321-2018.

Tian, J., Q. Wang, H. Ni, M. Wang, Y. Zhou, Y. Han, Z. Shen, S. Pongpiachan, N. Zhang, Z. Zhao, et al. 2019. Emission characteristics of primary brown carbon absorption from biomass and coal burning: Development of an optical emission inventory for China. *JGR. Atmospheres* 124 (3):1879–93. doi: 10.1029/2018JD029352.

UCAR. 2024. Quick TUV calculator. https://www.acom.ucar.edu/Models/TUV/Interactive_TUV/

van der Werf, G. R., J. T. Randerson, L. Giglio, G. J. Collatz, M. Mu, P. S. Kasibhatla, D. C. Morton, R. S. DeFries, Y. Jin, and T. T. van Leeuwen. 2010. Global fire emissions and the contribution of deforestation, savanna, forest, agricultural, and peat fires (1997–2009). *Atmos. Chem. Phys.* 10 (23):11707–35. doi: 10.5194/acp-10-11707-2010.

Wang, X., C. L. Heald, J. Liu, R. J. Weber, P. Campuzano-Jost, J. L. Jimenez, J. P. Schwarz, and A. E. Perring. 2018. Exploring the observational constraints on the simulation of brown carbon. *Atmos. Chem. Phys.* 18 (2):635–53. doi: 10.5194/acp-18-635-2018.

Wang, X., T. Liu, F. Bernard, X. Ding, S. Wen, Y. Zhang, Z. Zhang, Q. He, S. Lü, J. Chen, et al. 2014. Design and characterization of a smog chamber for studying gas-phase chemical mechanisms and aerosol formation. *Atmos. Meas. Tech.* 7 (1):301–13. doi: 10.5194/amt-7-301-2014.

Wang, Z., Y. Cheng, N. Ma, E. Mikhailov, U. Pöschl, and H. Su. 2017. Dependence of the hygroscopicity parameter κ on particle size, humidity and solute concentration: Implications for laboratory experiments, field measurements and model studies. *Atmos. Chem. Phys. Discuss.* 1–33. doi: 10.5194/acp-2017-253.

Washenfelder, R. A., J. M. Flores, C. A. Brock, S. S. Brown, and Y. Rudich. 2013. Broadband measurements of aerosol extinction in the ultraviolet spectral region. *Atmos. Meas. Tech.* 6 (4):861–77. doi: 10.5194/amt-6-861-2013.

West, C. P., A. P. S. Hettiyadura, A. Darmody, G. Mahamuni, J. Davis, I. Novosselov, and A. Laskin. 2020. Molecular composition and the optical properties of brown carbon generated by the ethane flame. *ACS Earth Space Chem.* 4 (7):1090–103. doi: 10.1021/acsearthspacechem.0c00095.

Williams, L. R., T. Onasch, D. Worsnop, R. Yokelson, P. Buseck, A. J. Sedlacek, III, R. Zaveri, Q. Zhang, and K. Adachi. 2018. *Understanding the evolution of biomass burning particles in the atmosphere: Analysis of BBOP data, laboratory experiments, and model integration*. Billerica, MA: Aerodyne Research, Inc.

Wong, J. P. S., M. Tsagkaraki, I. Tsiodra, N. Mihalopoulos, K. Violaki, M. Kanakidou, J. Sciare, A. Nenes, and R. J. Weber. 2019. Atmospheric evolution of molecular-weight-separated brown carbon from biomass burning. *Atmos. Chem. Phys.* 19 (11):7319–34. doi: 10.5194/acp-19-7319-2019.

Wong, J. P. S., A. Nenes, and R. J. Weber. 2017. Changes in light absorptivity of molecular weight separated brown carbon due to photolytic aging. *Environ. Sci. Technol.* 51 (15):8414–21. doi: 10.1021/acs.est.7b01739.

Xia, C., J. Sun, X. Hu, X. Shen, Y. Zhang, S. Zhang, J. Wang, Q. Liu, J. Lu, S. Liu, et al. 2023. Effects of hygroscopicity on aerosol optical properties and direct radiative forcing in Beijing: Based on two-year observations. *Sci. Total Environ.* 857 (Pt 1):159233. doi: 10.1016/j.scitotenv.2022.159233.

Yokelson, R. J., D. W. T. Griffith, and D. E. Ward. 1996. Open-path Fourier transform infrared studies of large-scale laboratory biomass fires. *J. Geophys. Res.* 101 (D15): 21067–80. doi: 10.1029/96JD01800.

Yoon, S.-C, and J. Kim. 2006. Influences of relative humidity on aerosol optical properties and aerosol radiative forcing during ACE-Asia. *Atmos. Environ.* 40 (23):4328–38. doi: 10.1016/j.atmosenv.2006.03.036.

You, B., Z. Zhang, A. Du, Y. Li, J. Sun, Z. Li, C. Chen, W. Zhou, W. Xu, L. Lei, et al. 2024. Seasonal characterization of chemical and optical properties of water-soluble organic aerosol in Beijing. *Sci. Total Environ.* 930:172508. doi: 10.1016/j.scitotenv.2024.172508.

Zeng, L., J. Dibb, E. Scheuer, J. M. Katich, J. P. Schwarz, I. Bourgeois, J. Peischl, T. Ryerson, C. Warneke, A. E. Perring, et al. 2022. Characteristics and evolution of brown carbon in western United States wildfires. *Atmos. Chem. Phys.* 22 (12):8009–36. doi: 10.5194/acp-22-8009-2022.

Zhang, A., Y. Wang, Y. Zhang, R. J. Weber, Y. Song, Z. Ke, and Y. Zou. 2020. Modeling the global radiative effect of brown carbon: A potentially larger heating source in the tropical free troposphere than black carbon. *Atmos. Chem. Phys.* 20 (4):1901–20. doi: 10.5194/acp-20-1901-2020.

Zhang, L., Z. Luo, W. Du, G. Li, G. Shen, H. Cheng, and S. Tao. 2020. Light absorption properties and absorption emission factors for indoor biomass burning. *Environ. Pollut.* 267:115652. doi: 10.1016/j.envpol.2020.115652.

Zhao, R., A. K. Y. Lee, L. Huang, X. Li, F. Yang, and J. P. D. Abbatt. 2015. Photochemical processing of aqueous atmospheric brown carbon. *Atmos. Chem. Phys.* 15 (11):6087–100. doi: 10.5194/acp-15-6087-2015.

Zhong, M., and M. Jang. 2014. Dynamic light absorption of biomass-burning organic carbon photochemically aged under natural sunlight. *Atmos. Chem. Phys.* 14 (3):1517–25. doi: 10.5194/acp-14-1517-2014.